



Article

Structural and Magnetic Properties of Co-Mn Codoped ZnO Nanoparticles Obtained by Microwave Solvothermal Synthesis

Jacek Wojnarowicz ^{1,*}, Myroslava Omelchenko ², Jacek Szczytko ², Tadeusz Chudoba ¹, Stanisław Gierlotka ¹, Andrzej Majhofer ², Andrzej Twardowski ² and Witold Lojkowski ¹

¹ Institute of High Pressure Physics, Polish Academy of Sciences, Sokolowska 29/37, 01-142 Warsaw, Poland; t.chudoba@labnano.pl (T.C.); xray@unipress.waw.pl (S.G.); w.lojkowski@labnano.pl (W.L.)

² Institute of Experimental Physics, Faculty of Physics, University of Warsaw, Pasteura 5, 02-093 Warsaw, Poland; myroslava.omelchenko@fuw.edu.pl (M.O.); jacek.szczytko@fuw.edu.pl (J.S.); andrzej.majhofer@fuw.edu.pl (A.M.); andrzej.twardowski@fuw.edu.pl (A.T.)

* Correspondence: j.wojnarowicz@labnano.pl; Tel.: +48-228-760-429

Received: 11 October 2018; Accepted: 29 October 2018; Published: 31 October 2018



Abstract: Zinc oxide nanoparticles codoped with Co²⁺ and Mn²⁺ ions (Zn_(1-x-y)Mn_xCo_yO NPs) were obtained for the first time by microwave solvothermal synthesis. The nominal content of Co²⁺ and Mn²⁺ in Zn_(1-x-y)Mn_xCo_yO NPs was x = y = 0, 1, 5, 10 and 15 mol % (the amount of both ions was equal). The precursors were obtained by dissolving zinc acetate dihydrate, manganese (II) acetate tetrahydrate and cobalt (II) acetate tetrahydrate in ethylene glycol. The morphology, phase purity, lattice parameters, dopants content, skeleton density, specific surface area, average particle size, average crystallite size, crystallite size distribution and magnetic properties of NPs were determined. The real content of dopants was up to 25.0% for Mn²⁺ and 80.5% for Co²⁺ of the nominal content. The colour of the samples changed from white to dark olive green in line with the increasing doping level. Uniform spherical NPs with wurtzite structure were obtained. The average size of NPs decreased from 29 nm to 21 nm in line with the increase in the dopant content. Brillouin type paramagnetism and an antiferromagnetic interaction between the magnetic ions was found for all samples, except for that with 15 mol % doping level, where a small ferromagnetic contribution was found. A review of the preparation methods of Co²⁺ and Mn²⁺ codoped ZnO is presented.

Keywords: zinc oxide; nanoparticles; codoping; cobalt (II) ions; manganese (II) ions; microwave solvothermal synthesis; structural properties; magnetic properties; dilute magnetic semiconductors

1. Introduction

Zinc oxide (ZnO) is a multi-functional material [1,2]. The ZnO structure that is thermodynamically stable at room temperature is wurtzite [3]. The ZnO is characterised by a wide band gap of 3.37 eV and a high exciton binding energy (60 meV), which permits the application of ZnO in electronics and optoelectronics [4–11]. The antibacterial and antifungal action of ZnO put ZnO NPs in the centre of interest in the fields of biomedicine and dentistry [11–22]. Research is in progress to find new applications of ZnO NPs in producing, for instance, solar cells [23,24], storage media [25], liquid crystals [26], nanostructured polymer composites [27], water filtration [28], photocatalysts [29–31], sensing applications [32,33], coatings for UV protection [34–36] and crop protection [37,38]. The development of the technologies of synthesis and modification of ZnO properties has made ZnO NPs the focus of spintronics [6,39].

Spintronics is the science of electron spin and the related magnetic moment in semiconductors. Many researchers share the view that the 21st century will be remembered as the age of spintronic

revolution due to the construction of the first spintronic devices for quantum computation or communication [40]. Spintronics enables the creation of next-generation optoelectronic devices and data carriers [41]. New materials, e.g., diluted magnetic semiconductors (DMS), where spin-polarised charge carriers can be obtained to enable performance of operations in spintronic devices, are being intensively sought. DMS are materials that are characterised by semiconductor (tunable conductivity) and ferromagnetic (controlled spin polarisation) properties.

Dietl et al. [42] discussed the Zener model of ferromagnetism in zinc-blend magnetic semiconductors including ZnO by calculating Curie temperature T_c higher than 100 K. Doped ZnO has long been considered a promising material for applications as DMS as a result of theoretical calculations, implying that doped ZnO might display ferromagnetic properties at the room temperature [43,44]. Additionally, such ZnO properties as the band gap value and the conductivity could be controlled through doping ZnO NPs with ions of transition metals (e.g., Co, Mn, Cr, Ni, Fe, V). The issue of doped ZnO NPs has been quite extensively examined by various research groups [6,44–47].

ZnO NPs doped with Co^{2+} ($\text{Zn}_{(1-y)}\text{Co}_y\text{O}$) and Mn^{2+} ($\text{Zn}_{(1-x)}\text{Mn}_x\text{O}$) ions have gained much interest from scientists [4,6]. Despite numerous studies, the magnetic properties of $\text{Zn}_{(1-x)}\text{Mn}_x\text{O}$ NPs and $\text{Zn}_{(1-y)}\text{Co}_y\text{O}$ NPs have been a fairly controversial subject so far [45–69]. The nature of the origin of the ferromagnetic properties of doped ZnO NPs has not been unambiguously described yet. Most researchers explain a change in the magnetic properties of $\text{Zn}_{(1-x)}\text{Mn}_x\text{O}$ NPs and $\text{Zn}_{(1-y)}\text{Co}_y\text{O}$ NPs with the formation of, e.g., a secondary phase such as Co metal clusters, $\text{Co}(\text{OH})_2$, CoO , Co_3O_4 , Co_2O_4 , Mn_2O_3 , Mn_3O_4 , ZnMnO_3 [48–60] and a spinel phase (ZnMn_2O_4 , ZnCo_2O_4) [53,54,57–64], which are characterised by different magnetic properties (Table 1). However, a change in the magnetic properties of doped ZnO NPs, apart from a change in the level of the oxidation state of dopants and the presence of foreign phases, can also be explained by the presence of oxygen vacancies, the formation of dopant clusters, the exchange interaction between the local spin-polarised electrons and associated with specific defects and adsorbed elements at the surface of the NPs [66–71]. Martínez et al. [72], in turn, correlated the role of the microstructure with the change of the magnetic properties of $\text{Zn}_{(1-y)}\text{Co}_y\text{O}$ NPs, which demonstrates the complex nature of the magnetic properties of NPs. Based on the results of our own research [73], we believe that if the synthesis method employed permits the achievement of uniform substitution of Zn^{2+} ions in the ZnO crystalline lattice with dopant ions (Co^{2+} or Mn^{2+}), such a material will be paramagnetic with some antiferromagnetic coupling. Currently, new methods of modifying ZnO properties are being sought to enable obtaining ZnO properties that satisfy the criteria of a DMS [46]. One of the solutions could be, e.g., codoping of ZnO with ions of Mn^{2+} and Co^{2+} ($\text{Zn}_{(1-x-y)}\text{Mn}_x\text{Co}_y\text{O}$). Codoping is a promising strategy that enables an effective modification of the magnetic and electronic properties of DMS materials. Research concerning codoping has been carried out for more than 20 years now [74]. It is believed that codoping might overcome the difficulties in bipolar doping and compensation in semiconductors [74]. Thanks to codoping, it is possible to increase the solubility of dopants, improve the stability of the expected defects, increase the carrier mobility and increase the activation rate by lowering the ionisation energy of acceptors and donors [74,75].

Table 1. Magnetic properties of the secondary phase observed in Mn²⁺-doped ZnO and Co²⁺-doped ZnO.

Phase	Magnetic Properties	Reference
Mn	Antiferromagnetic	[76]
MnO	Antiferromagnetic	[77]
MnO ₂	Antiferromagnetic	[77]
Mn ₂ O ₃	Antiferromagnetic	[77]
Mn ₃ O ₄	Ferromagnetic	[77]
ZnMnO ₃	Paramagnetic	[78,79]
ZnMn ₂ O ₄	Ferromagnetic	[80]
Mn(OH) ₂	Antiferromagnetic	[81]
Co	Ferromagnetic	[82]
Co ²⁺ cluster	Ferromagnetic	[83]
CoO	Antiferromagnetic	[84]
Co ₃ O ₄	Antiferromagnetic	[85]
Co ₂ O ₃	Antiferromagnetic	[86]
ZnCo ₂ O ₄	Ferromagnetic	[87]
Co(OH) ₂	Paramagnetic	[88]

The relevant literature has reported a dozen or so methods of obtaining Zn_(1-x-y)Mn_xCo_yO nanostructures, an overview of which is presented in Table 2.

Table 2. Summary of methods of obtaining Mn²⁺-and Co²⁺-codoped ZnO.

Method	Substrates	Conditions during Preparation	Morphology; Magnetic Properties; Maximum Content of Dopants	Reference
pulsed laser deposition	ZnO, Co ₃ O ₄ with MnO ₂	from 400 °C to 600 °C and a low oxygen pressure (5×10^{-5} Pa).	films; room-temperature ferromagnetism; Zn _{0.7} Mn _{0.15} Co _{0.15} O	[89]
radio-frequency magnetron co-sputtering and annealing	Zn _{0.95} Mn _{0.05} O, Zn _{0.80} Co _{0.20} O	550 °C in argon ambient; 400 °C, 600 °C, 800 °C and 900 °C for 1 h in air	films; ferromagnetic and paramagnetic behaviour; Zn _{0.90} Mn _{0.03} Co _{0.07} O	[90–92]
autocombustion	Zn(NO ₃) ₂ ·6H ₂ O, Co(NO ₃) ₂ ·6H ₂ O, Mn(NO ₃) ₂ , NH ₂ CH ₂ COOH and H ₂ O	-	nanoparticles; ferromagnetic; Zn _{0.96} Mn _{0.02} Co _{0.02} O	[93]
thermal plasma and annealing	zinc, cobalt and manganese metal powders	450 °C, 550 °C and 650 °C for 1 h, atmospheric air	Particles;	[94,95]
thermal evaporation	Zn powders, MnCl ₂ ·4H ₂ O, CoCl ₂ ·6H ₂ O	500 °C with a constant argon flow of 50 sccm	nanowires (50–200 nm and lengths up to several tens of microns)	[96]
thermal decomposition	Zn(Ac) ₂ ·2H ₂ O, Mn(Ac) ₂ ·4H ₂ O, Co(Ac) ₂ ·4H ₂ O and C ₁₆ H ₃₃ NH ₂ and C ₄ H ₉ PO(OH) ₂	at 300 °C under a constant nitrogen flow	nanocrystals (7 nm); room temperature ferromagnetism	[97]
thermal diffusion	Zn(NO ₃) ₂ ·6H ₂ O, C ₆ H ₁₂ N ₄ , Mn and Co (metal powders)	at 850 °C in a vacuum at about 1×10^{-3} Torr.	nanorods (1–2 μm length and 80–200 nm diameter)	[98]
chemical route and annealing	Zn(Ac) ₂ ·2H ₂ O, Mn(Ac) ₂ ·4H ₂ O, Co(Ac) ₂ ·4H ₂ O and ethylene glycol	200 °C for 3 h; 600 °C in (Ar95% H5%) and in air.	nanoparticles (25 nm); paramagnetic and ferromagnetic behaviour; Zn _{0.94} Mn _{0.04} Co _{0.02} O, Zn _{0.94} Mn _{0.02} Co _{0.04} O	[99]
solid state reaction and calcination	ZnO was mixed with MnCO ₃ and Co ₂ O (the mixtures were ball milled)	2 h in 1000 °C, 1050 °C, 1100 °C, 1150 °C, and 1200 °C in atmospheric air	particles; Zn _{0.94} Mn _{0.01} Co _{0.05} O	[100]
solid state reaction and calcination	ZnO was mixed with Mn and Co (metal powders) with the assistance citric acid	1100 °C for 7 day in air	room temperature ferromagnetism; Zn _{0.90} Mn _{0.05} Co _{0.05} O	[101]

Table 2. Cont.

Method	Substrates	Conditions during Preparation	Morphology; Magnetic Properties; Maximum Content of Dopants	Reference
sol-gel	Zn(Ac) ₂ ·2H ₂ O, Mn(Ac) ₂ ·4H ₂ O, Co(Ac) ₂ ·4H ₂ O ethanol solution as a solvent, and DEA as a stabilizing agent	500 °C for 1 h in O ₂ atmosphere,	particles; exhibited ferromagnetic character; Zn _{0.94} Mn _{0.04} Co _{0.02} O	[102]
	Zn(Ac) ₂ ·2H ₂ O, Mn(Ac) ₂ ·4H ₂ O, Co(Ac) ₂ ·4H ₂ O, NaOH, water and N,N-dimethylformamide,	500 °C for 1 h in atmospheric air	nanoparticles; ferromagnetism behaviour; Zn _{0.7} Co _{0.15} Mn _{0.15} O	[103]
	Zn(Ac) ₂ ·2H ₂ O, Mn(Ac) ₂ ·4H ₂ O, Co(Ac) ₂ ·4H ₂ O, N,N dimethyl-formamide (DMF)	500 °C for 4 h in atmospheric air	nanoparticles (20–30 nm); Zn _{0.88} Mn _{0.04} Co _{0.08} O	[104]
microwave assisted combustion synthesis	Mn(NO ₃) ₂ ·4H ₂ O, Co(NO ₃) ₆ ·H ₂ O, Zn(NO ₃) ₂ ·6H ₂ O, water, using urea as a fuel	800 W for 15 min (kitchen type microwave)	nanoparticles (24 nm); paramagnetic and ferromagnetic behaviour; Zn _{0.70} Mn _{0.20} Co _{0.10} O	[105]
	Mn(NO ₃) ₂ ·4H ₂ O, Co(NO ₃) ₆ ·H ₂ O, Zn(NO ₃) ₂ ·6H ₂ O, water, using urea as a fuel	1000 W for 20 min (kitchen type microwave)	nanoparticles (31 nm); room temperature ferromagnetism; Zn _{0.80} Mn _{0.10} Co _{0.10} O	[106]
co-precipitation and calcination	Zn(Ac) ₂ ·2H ₂ O, Mn(Ac) ₂ ·4H ₂ O, Co(Ac) ₂ ·4H ₂ O, (COOH) ₂ ·2H ₂ O	350 °C, 500 °C and 650 °C in atmospheric air	nanoparticles; ferromagnetism behaviour Zn _{0.90} Mn _{0.05} Co _{0.05} O	[107–109]
	Zn(Ac) ₂ ·2H ₂ O, MnCl ₄ ·4H ₂ O, CoCl ₂ ·6H ₂ O, NH ₄ OH	400 °C for 3 h in atmospheric air	nanoparticles (28 nm); ferromagnetic behaviour; Zn _{0.98} Mn _{0.01} Co _{0.01} O	[110]
	Zn(Ac) ₂ ·2H ₂ O, Mn(Ac) ₂ ·4H ₂ O, Co(Ac) ₂ ·4H ₂ O, Na(OH), water	550 °C for 3 h in atmospheric air	nanoparticles (20 nm); ferromagnetic behaviour; Zn _{0.85} Mn _{0.10} Co _{0.05} O	[111]
	Mn(NO ₃) ₂ ·4H ₂ O, Co(NO ₃) ₆ ·H ₂ O, Zn(NO ₃) ₂ ·6H ₂ O, LiOH·H ₂ O, H ₂ O, C ₂ H ₅ OH	300 °C for 3 h in atmospheric air	nanoparticles; Zn _{0.92} Co _{0.02} Mn _{0.06} O	[112]
	Zn(Ac) ₂ ·2H ₂ O, Mn(Ac) ₂ ·4H ₂ O, Co(Ac) ₂ ·4H ₂ O, NH ₄ OH, H ₂ O	750 °C for 2 h in atmospheric air	nanoparticles (15–17 nm); Zn _{0.92} Mn _{0.04} Co _{0.04} O	[113,114]
electrochemical	ZnCl ₂ , MnCl ₂ , CoCl ₂ , KCl, tartaric acid	densities of electrodepositioning in the range of 0.5–2.0 mA/cm ²	nanorod (diameters: 50–100 nm, no longer than 500 nm)	[115]

The magnetic properties of codoped ZnO depend chiefly on the method of obtaining it, the synthesis parameters and the sample preparation process (Table 2). Most authors modified the properties of the obtained $Zn_{(1-x-y)}Mn_xCo_yO$ samples by selecting the temperature and gas atmosphere of the applied method or by soaking the samples additionally. An appropriate selection of the parameters for obtaining or preparing $Zn_{(1-x-y)}Mn_xCo_yO$ samples permits the oxidation or reduction of dopant ions, which might result in the formation of a secondary phase of, e.g., dopant oxides and oxygen vacancies. A good example might be a study of Naeem et al. [99], where $Zn_{(1-x-y)}Mn_xCo_yO$ NPs were obtained with the use of a chemical route and then were deliberately soaked at a temperature of 600 °C in an oxidising atmosphere and a reducing atmosphere. It was only $Zn_{(1-x-y)}Mn_xCo_yO$ NP samples soaked in a reducing atmosphere that displayed ferromagnetic properties; their nature was explained by the formation of oxygen vacancies because Naeem et al. did not observe any foreign phase inclusions within the detection limit of the X-ray diffraction method. In order to understand the nature of the magnetic properties of $Zn_{(1-x-y)}Mn_xCo_yO$, the first-principles method based on the density functional theory is employed for their analysis [116–118].

Microwave solvothermal synthesis (MSS) has not been used for obtaining $Zn_{(1-x-y)}Mn_xCo_yO$ NPs yet. Microwave technology is successfully applied for obtaining nanomaterials [119–129], including diverse nanostructures of ZnO [130–142]. The increased popularity of microwave-driven syntheses mainly arises from the decreasing prices of microwave reactors and the emergence of new reactor designs [143–147]. The main advantages of microwave heating in the case of ZnO NPs syntheses include:

- reduction of the synthesis duration in comparison with conventional heating methods,
- high homogeneity of NPs and narrow size distribution resulting from a small temperature gradient in the reaction vessel,
- high product purity.

Our research conducted to date has shown that the microwave solvothermal synthesis of ZnO enables:

- obtaining homogenous ZnO NPs with controlled size from circa 15 nm to 120 nm [140,141];
- controlling the average size of ZnO NPs aggregates of 60, 90 and 120 nm at the same time preserving the constant size of single NPs, which are sized 27 nm [148];
- obtaining homogenous ZnO NPs doped with Co^{2+} or Mn^{2+} ions [73,149,150];
- obtaining ZnO NPs doped with Co^{2+} ions with controlled particle size between at least 28 nm and 53 nm [151].

The aim of this study is to prove that the microwave solvothermal synthesis enables obtaining homogeneous spherical $Zn_{(1-x-y)}Mn_xCo_yO$ NPs with paramagnetic properties.

2. Materials and Methods

2.1. Substrates

Reagents used: zinc acetate dihydrate ($Zn(CH_3COO)_2 \cdot 2H_2O$, Zn(Ac)₂·2H₂O analytically pure, Chempur, Piekary Śląskie, Poland); manganese (II) acetate tetrahydrate ($Mn(CH_3COO)_2 \cdot 4H_2O$, Mn(Ac)₂·4H₂O, analytically pure, Chempur, Piekary Śląskie, Poland), cobalt (II) acetate tetrahydrate ($Co(CH_3COO)_2 \cdot 4H_2O$, Co(Ac)₂·4H₂O pure, Sigma-Aldrich, St. Louis, MO, USA); ethylene glycol (EG, ethane-1,2-diol, C₂H₄(OH)₂, pure, Chempur, Piekary Śląskie, Poland); deionised water (H₂O) (specific conductance < 0.1 μS/cm, HLP 20UV, Hydrolab, Straszyn, Poland). The reagents were not subjected to any purification processes and were used as received. Only deionised water was used in the sample preparation process.

2.2. Synthesis of $Zn_{(1-x-y)}Mn_xCo_yO$ NPs

$Zn_{(1-x-y)}Mn_xCo_yO$ NPs were obtained with the use of the MSS method in accordance with the procedure described in our earlier publications [73,149–152]. Precursors of $Zn_{(1-x-y)}Mn_xCo_yO$ were prepared by dissolving mixtures of crystalline cobalt acetate, manganese acetate, and zinc acetate in ethylene glycol. The composition of $Zn_{(1-x-y)}Mn_xCo_yO$ NPs precursors summarised in Table 1 was calculated based on Equations (1) and (2), with the molar concentration of zinc acetate in ethylene glycol being constant and amounting to 0.3037 mol/dm^3 .

$$x_{Mn^{2+}} = \frac{n_{Mn^{2+}}}{n_{Zn^{2+}} + n_{Mn^{2+}} + n_{Co^{2+}}} \quad (1)$$

$$y_{Co^{2+}} = \frac{n_{Co^{2+}}}{n_{Zn^{2+}} + n_{Mn^{2+}} + n_{Co^{2+}}} \quad (2)$$

Precursor solutions (Table 3) were obtained by dissolving strictly defined compositions of mixtures of the acetates in glycol (150 mL) using a hot-plate magnetic stirrer (70 °C, 450 rpm, SLR, SI Analytics GmbH, Mainz, Germany). After the acetates dissolved, each solution was poured into a bottle (250 mL, PP), sealed and cooled down until it reached the ambient temperature.

Table 3. Compositions (nominal content) of precursors of $Zn_{(1-x-y)}Mn_xCo_yO$ synthesis.

Name of Precursor	$Cm_{Zn(Ac)2 \cdot 2H_2O}$ (mol/dm ³)	$Cm_{Mn(Ac)2 \cdot 4H_2O}$ (mol/dm ³)	$Cm_{Co(Ac)2 \cdot 4H_2O}$ (mol/dm ³)
ZnO	0.3037	0	0
$Zn_{0.98}Mn_{0.01}Co_{0.01}O$	0.3037	0.0031	0.0031
$Zn_{0.90}Mn_{0.05}Co_{0.05}O$	0.3037	0.0169	0.0169
$Zn_{0.80}Mn_{0.10}Co_{0.10}O$	0.3037	0.0380	0.0380
$Zn_{0.70}Mn_{0.15}Co_{0.15}O$	0.3037	0.0651	0.0651

The parameters of NPs syntheses carried out in a microwave reactor (Model 02-02600 W, 2.45 GHz, ERTEC, Poland) were as follows: volume of the precursor poured into a Teflon reaction container—75 mL, heating duration—25 min; maximum temperature of the bottom of the outer wall of the reaction vessel [140]— $190 \pm 5 \text{ }^\circ\text{C}$; microwave power—100%, cool-down duration—20 min. The reaction duration was chosen based on our earlier research concerning the optimisation of parameters of the microwave solvothermal synthesis of ZnO NPs in ethylene glycol. Our primary assumption for the optimisation was to achieve the maximum reaction efficiency, while in the case of a reaction duration of 25 min the efficiency of zinc acetate conversion with identical synthesis parameters was circa 100% [141]. These setpoints of synthesis parameters were entered using the reactor's control panel window (see the Supplementary Materials). An example profile of the course of the microwave solvothermal synthesis in the reactor model 02-02 is presented in Figure 1. The microwave heating in the employed reactor can be divided into the following stages:

1. Continuous microwave heating of the feedstock until the preset maximum temperature is reached (T_{max})— $195 \text{ }^\circ\text{C}$.
2. Once the feedstock reaches the maximum temperature of $195 \text{ }^\circ\text{C}$, the reactor's controller switches off the microwave heating and the feedstock temperature drops to the preset minimum temperature (T_{min})— $185 \text{ }^\circ\text{C}$.
3. Once the feedstock reaches $T_{min} \text{ } 185 \text{ }^\circ\text{C}$, the reactor's controller switches on the continuous microwave heating and re-heats the sample to $T_{max} \text{ } 195 \text{ }^\circ\text{C}$.
4. Cyclic repetition of stages 2 and 3 until the preset reaction duration of 25 min is reached.
5. The reactor is cooled down by activating cold water flow in the metal body, inside which the Teflon reaction vessel containing the obtained post-reaction suspended matter is placed.

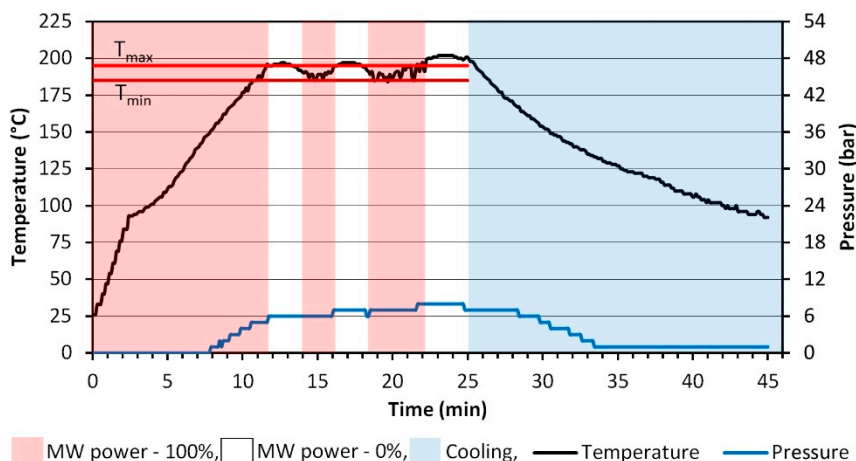


Figure 1. Diagram showing the course of the microwave synthesis of codoped ZnO NPs and undoped ZnO NPs on the example of $Zn_{0.98}Mn_{0.01}Co_{0.01}O$ sample. Experimental data obtained in the microwave reactor Model 02-02.

The synthesis of ZnO NPs codoped with Mn^{2+} and Co^{2+} ions in EG is presented by Equation (3):



Post-reaction suspended matter was centrifuged (MPW-350, MPW Med Instruments, Warsaw, Poland) and the supernatants were decanted. Afterwards, the sediments were rinsed intensively three times with water and centrifuged. Fifty millilitres of water were added to the obtained pastes; they were intensively stirred and then cooled down with liquid nitrogen and dried in a freeze dryer (Lyovac GT-2, SRK Systemtechnik GmbH, Riedstadt, Germany).

2.3. Characterisation Methods

The measurement procedures employed were described in our earlier publications [149,151]. The analysis of the phase composition was performed with the X-ray diffraction method (XRD) (2 theta from 10° to 150° , room temperature, $CuK_{\alpha 1}$, X'Pert PRO, Panalytical, The Netherlands). The parameters of the crystalline lattice, a and c , were determined by the Rietveld method in Fityk software, version 0.9.8. Crystallite size was calculated by means of Scherrer's formula [149] and an analysis of the profile of XRD peaks with the FW15/45M method [153–155], which also enabled the calculation of the crystallite size distribution.

The morphology of NPs was defined using scanning electron microscopy (SEM) (ZEISS, Ultra Plus, Oberkochen, Germany).

Density was measured using a helium pycnometer at a temperature of $24 \pm 1^\circ C$ (ISO 12154:2014, AccuPyc II 1340 FoamPyc V1.06, Micromeritics, Norcross, GA, USA).

The specific surface area of NPs was determined through an analysis of nitrogen adsorption isotherm by the BET (Brunauer-Emmett-Teller) method (ISO 9277:2010, Gemini 2360, V 2.01, Micromeritics). Based on the results of the specific surface area and density, the average particle size was calculated with the assumption that all particles were spherical and identical [149].

The chemical composition of the samples dissolved in nitric acid (V) was analysed with the use of argon inductively coupled plasma optical emission spectrometry (ICP-OES) (Thermo Fisher Scientific, iCAP model 6000, Waltham, MA, USA) [73]. The quantitative microanalysis of the Zn, Mn and Co content in the pressed NP samples was performed using energy-dispersive spectrometry (EDS) (Quantax 400, Bruker, Billerica, MA, USA) [151].

The colour analysis by means of the Red-Green-Blue (RGB; value: 0 to 1023) and Hue-Saturation-Luminance (HSL; value: 0 to 1000) colour model was carried out with the RGB-2000

metric by VOLTcraft (Conrad Electronic SE, Wernberg-Köblitz, Germany) in accordance with the manufacturer's recommendations.

The magnetisation measurements are performed with the use of a SQUID-type magnetometer (liquid helium cooled MPMSXL device manufactured by Quantum Design, Inc., San Diego, CA, USA) in the temperature range 2–300 K and magnetic fields up to 7 T.

3. Results and Discussion

3.1. Morphology

Figures 2 and 3 present selected representative SEM images of $Zn_{(1-x-y)}Mn_xCo_yO$ NP samples. An impact of the content of dopants on the morphology of $Zn_{(1-x-y)}Mn_xCo_yO$ is noticeable. Powders of ZnO and $Zn_{(0.98)}Mn_{0.01}Co_{0.01}O$ were composed of loose homogeneous spherical particles sized 20–50 nm. Powders of $Zn_{0.90}Co_{0.05}Mn_{0.05}O$ and $Zn_{0.8}Co_{0.1}Mn_{0.1}O$, in turn, were composed of compact homogeneous spherical NPs sized 20–40 nm, which formed conglomerates sized between 1 μm and 3 μm resembling a “cauliflower” in terms of shape and structure. A similar impact of a dopant on a change in NPs morphology was observed in our earlier studies on doped ZnO [149,151]. In order to eliminate the effect of aggregation of the obtained $Zn_{(1-x-y)}Mn_xCo_yO$ NPs, the synthesis parameters must be individually optimised for each composition of $Zn_{(1-x-y)}Mn_xCo_yO$ NPs. We have shown that microwave solvothermal synthesis permits controlling the size of ZnO NPs aggregates through a change of the microwave power used for ZnO NPs synthesis [148]. Zhang et al. [156] described the impact of a change in the solvothermal synthesis temperature on the size of ZnO NPs aggregates.

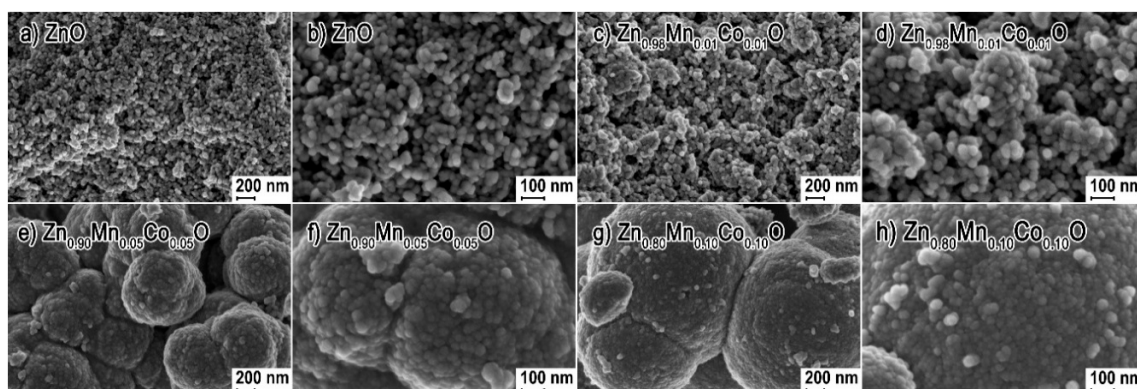


Figure 2. SEM images of NPs: (a,b) ZnO; (c,d) $Zn_{0.98}Co_{0.01}Mn_{0.01}O$; (e,f) $Zn_{0.90}Co_{0.05}Mn_{0.05}O$; (g,h) $Zn_{0.8}Co_{0.1}Mn_{0.1}O$.

Figure 3 presents the morphology of $Zn_{0.70}Co_{0.15}Mn_{0.15}O$ powder. SEM images show two products of synthesis: ZnO NPs aggregates, and a lamellar structure, which might be an unreacted intermediate in the form of hydroxide metal acetates with the general formula of $M_5(OH)_{(10-z)}(CH_3COO)_z \cdot nH_2O$, where $M = (Zn, Co \text{ and } Mn)$ [157], or a compound of codoped hydroxide metal acetates $Zn_{5(1-x-y)}Mn_{(5x)}Co_{(5y)}(OH)_{(10-z)}(CH_3COO)_z \cdot nH_2O$ [141,151]. Information regarding the phase composition of the $Zn_{0.70}Co_{0.15}Mn_{0.15}O$ sample will be provided by XRD. The product prevalent in the obtained $Zn_{0.70}Co_{0.15}Mn_{0.15}O$ sample is NPs, which is illustrated by the SEM image in Figure 3c.

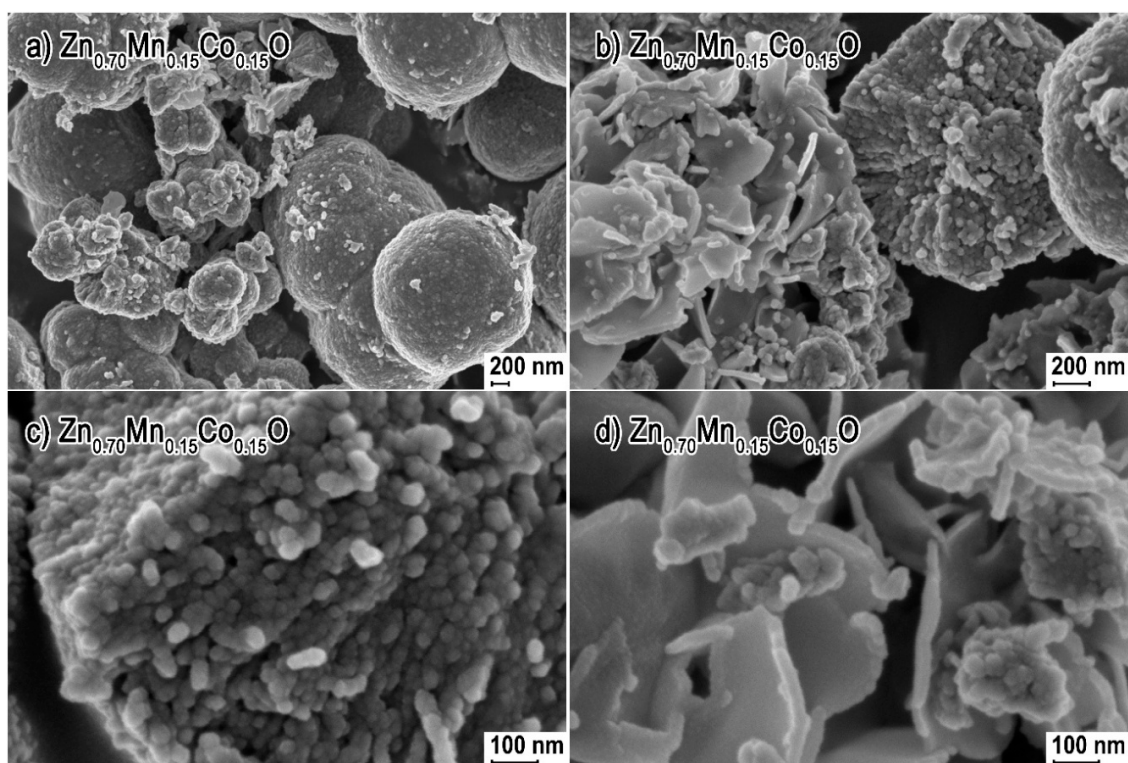


Figure 3. SEM images of NPs: (a–d) $\text{Zn}_{0.7}\text{Co}_{0.15}\text{Mn}_{0.15}\text{O}$.

3.2. Phase Composition and Lattice Parameters

Despite the presence of the lamellar structure visible in SEM images in the $\text{Zn}_{0.7}\text{Co}_{0.15}\text{Mn}_{0.15}\text{O}$ sample, all diffraction peaks in Figure 4 were attributed exclusively to the hexagonal phase ZnO (JCPDS No. 36-1451). The XRD test did not show the presence of the secondary phase, which could be $\text{M}_5(\text{OH})_{(10-z)}(\text{CH}_3\text{COO})_z \cdot n\text{H}_2\text{O}$ (lamellar structure) [157].

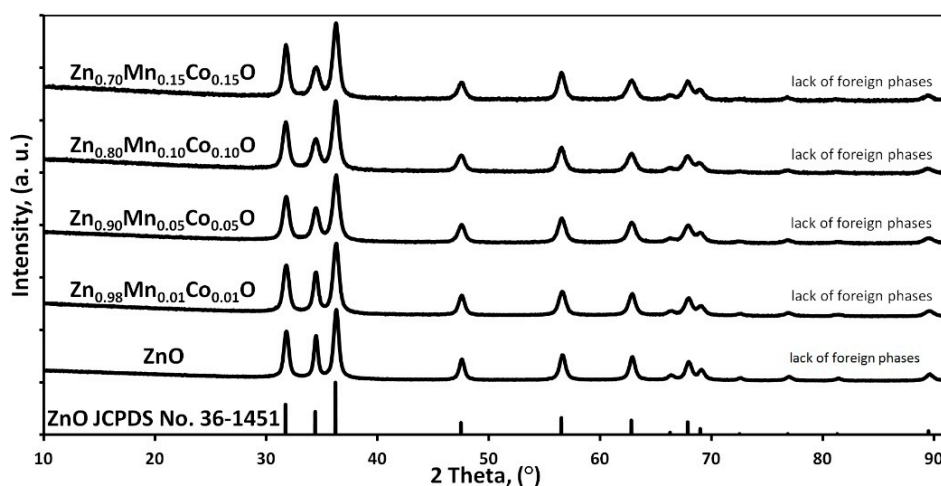


Figure 4. XRD diffraction patterns of $\text{Zn}_{(1-x-y)}\text{Mn}_x\text{Co}_y\text{O}$ NPs (where $x = y$), with the nominal content of dopants in the solution being 0, 1, 5, 10, 15 mol %.

The hexagonal phase of $\text{M}_5(\text{OH})_{(10-z)}(\text{CH}_3\text{COO})_z \cdot n\text{H}_2\text{O}$ has a diffraction peak below 10° (2 theta angle) [141]. In order to verify the presence of a foreign phase in the $\text{Zn}_{0.7}\text{Co}_{0.15}\text{Mn}_{0.15}\text{O}$ sample, XRD measurement was performed again with the range from 5° to 100° (Figure 5). All diffraction peaks in

Figure 5 were attributed exclusively to the hexagonal phase ZnO (JCPDS No. 36-1451). The absence of the secondary phase (Figure 3) in XRD results may mean that:

- the amount of the secondary phase was below the detection limit of the XRD method,
- the secondary phase was an amorphous material,
- the secondary phase is lamellar-shaped ZnO.

At this stage of the research, we are unable to identify what the lamellar structure product in the $\text{Zn}_{0.7}\text{Co}_{0.15}\text{Mn}_{0.15}\text{O}$ sample is (Figure 3) and we do not know whether its presence can be eliminated through optimisation of microwave solvothermal synthesis processes. This requires further research.

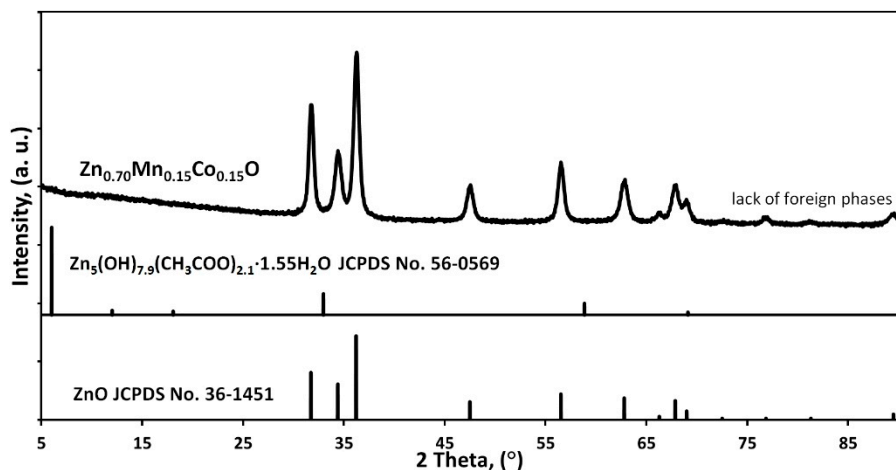


Figure 5. XRD diffraction pattern of the $\text{Zn}_{0.7}\text{Co}_{0.15}\text{Mn}_{0.15}\text{O}$ sample, and its comparison with the standard pattern of $\text{Zn}_5(\text{OH})_{7.9}(\text{CH}_3\text{COO})_{2.1} \cdot 1.55\text{H}_2\text{O}$ (JCPDS No. 56-0569) and ZnO (JCPDS No. 36-1451).

Theorem-type environments (including propositions, lemmas, corollaries, etc.) can be formatted as follows: ZnO is characterised by the hexagonal wurtzite structure (295 K, h-ZnO space group P63mc) with the lattice parameters of $a = 3.2498 \text{ \AA}$ and $c = 5.2066 \text{ \AA}$ [6], while the c/a lattice parameter ratio in ZnO is 1.6021 and is close to the c/a value = 1.6330 for the theoretical close-packed hexagonal structure (hcp) [151,158]. The ionic radius of Zn^{2+} is 0.74 \AA [159]. Manganese oxide (II) MnO has a cubic rock salt structure (295 K, c-MnO, space group Oh5—Fm3m) with the lattice parameter of $a = 4.4475 \text{ \AA}$ [160], and the ionic radius of Mn^{2+} is 0.83 \AA [161]. Cobalt oxide (II) CoO crystallises in two crystalline phases: cubic rock salt CoO (295 K, c-CoO, space group Fm3m) with the lattice parameter of $a = 4.2581 \text{ \AA}$, and hexagonal wurtzite CoO (77 K, h-CoO, space group P63mc) with lattice parameters of $a = 5.183 \text{ \AA}$ and $c = 3.017 \text{ \AA}$ [160]. The ionic radius of Co^{2+} is 0.745 \AA [162].

The results of our earlier studies [73,149] proved that the lattice parameters a and c in ZnO change in line with the change in Co^{2+} or Mn^{2+} ion content, which we explained with the impact of changes in the values of ion radii of dopants in relation to Zn^{2+} . However, each dopant gave rise to a distinct change in the value of the lattice parameters of doped ZnO depending on the content and type. For Co^{2+} dopant ions, whose ion radius is almost identical to that of Zn^{2+} , the value of a lattice parameter in $\text{Zn}_{(1-y)}\text{Co}_y\text{O}$ samples grew in line with the increase in the dopant content from 1% to 15% [73]. The value of the c lattice parameter, in turn, grew when the nominal dopant content ranged from 1% to 5%, and dropped when the content was 5 to 15%. In the case of the dopant of Mn^{2+} ions, where their ionic radius is greater than Zn^{2+} radius by as much as 0.09 \AA , both lattice parameters, a and c , in $\text{Zn}_{(1-x)}\text{Mn}_x\text{O}$ samples increased their values within the dopant content range of 1 to 25 mol % [149].

The calculated a and c lattice parameters of $\text{Zn}_{(1-x-y)}\text{Mn}_x\text{Co}_y\text{O}$ samples are presented in Table 4 and in Figure 6. The value of both lattice parameters a and c grew in line with the increase in the

content of Mn^{2+} and Co^{2+} dopants in ZnO (Figure 6). Table 4 also presents the lattice parameters of $Zn_{0.85}Mn_{0.15}O$ NPs and $Zn_{0.85}Co_{0.15}O$ NPs as comparative samples for the $Zn_{0.70}Mn_{0.15}Co_{0.15}O$ sample. According to our assumptions, the principal impact on the value of ZnO lattice parameters was exerted by the dopant with the greater ionic radius since a and c lattice parameters for the $Zn_{0.70}Mn_{0.15}Co_{0.15}O$ sample are comparable to the values for the $Zn_{0.85}Mn_{0.15}O$ sample. The change in a and c lattice parameters in the obtained $Zn_{(1-x-y)}Mn_xCo_yO$ samples proves an effective substitution of Zn^{2+} ions with Mn^{2+} and Co^{2+} dopant ions in the ZnO crystalline lattice. Similar dependencies on changes to Mn-Co codoped ZnO lattice parameters were described by Adbullahi et al. [105].

Table 4. Lattice parameters and ratio of lattice parameters of the obtained $Zn_{(1-x-y)}Mn_xCo_yO$ NPs.

Sample	Lattice Parameters		Ratio of Lattice Parameters c/a	In hcp Structure, ZnO, Ratio of Lattice Parameters c/a
	$a \pm \sigma$, [Å]	$c \pm \sigma$, [Å]		
ZnO (JCPDS No. 36-1451)	3.2498	5.2066	1.6021	
ZnO	3.2508	5.2074	1.6017	
$Zn_{0.98}Mn_{0.01}Co_{0.01}O$	3.2520	5.2083	1.6010	
$Zn_{0.90}Mn_{0.05}Co_{0.05}O$	3.2547	5.2107	1.6007	1.6330
$Zn_{0.80}Mn_{0.10}Co_{0.10}O$	3.2563	5.2122	1.6007	
$Zn_{0.70}Mn_{0.15}Co_{0.15}O$	3.2569	5.2134	1.6007	
$Zn_{0.85}Mn_{0.15}O$ [149]	3.2564	5.2138	1.6011	
$Zn_{0.85}Co_{0.15}O$ [73]	3.2520	5.2040	1.6003	

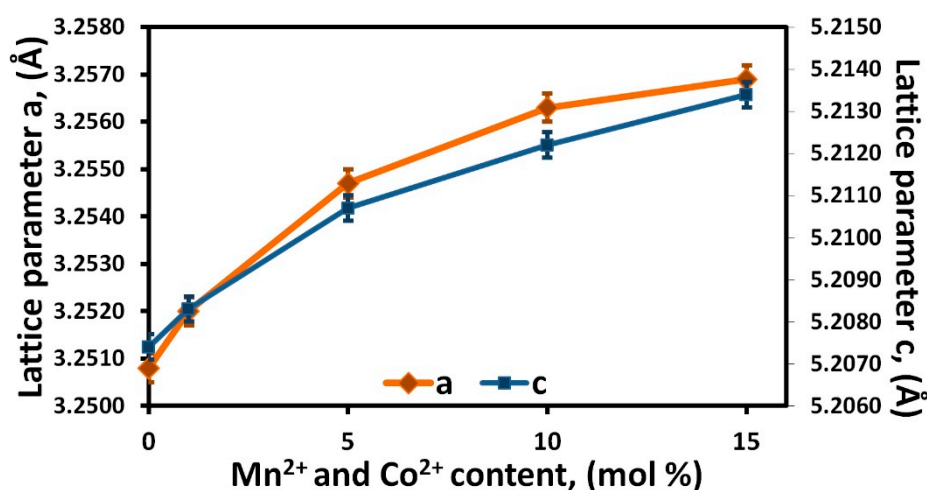


Figure 6. Lattice parameters versus nominal dopants content of $Zn_{(1-x-y)}Mn_xCo_yO$ NP samples.

3.3. Impact of Chemical Composition on the Colour of Codoped ZnO NPs

The results of the dopant content analysis are presented in Table 5. The differences between the results of the analysis carried out by the EDS method and the ICP-OES method arise from the sensitivity, accuracy and limitations of these analytical techniques as regards the quantitative determination of manganese, cobalt and zinc. The NP samples for the EDS analysis were pressed to form pastilles so that the sample surface was flat and smooth and the porosity of the examined material was reduced as much as possible (ISO 22309:2011). The ICP method is considered a source of the most representative results owing to its numerous advantages, e.g., low detection limits, a wide linear dynamic range, high precision [163]. Our interesting findings include efficiencies of doping for the obtained samples (Table 6). In line with the increase in the nominal contents of two dopants in precursor solutions, the efficiency of doping with Mn^{2+} ions decreased and at the same time the efficiency of doping with Co^{2+} ions in codoped ZnO NPs increased. The achieved low efficiency of doping with Mn^{2+} , which was between 16% and 25%, can be explained by the difference in the sizes of the ionic radii of Mn^{2+} and Zn^{2+}

being 0.09 Å. The efficiency of doping with Co^{2+} ions, in turn, was as many as 3–4 times greater than the efficiency of doping with Mn^{2+} ions, which is explained by the negligible difference in the values of Co^{2+} and Zn^{2+} ionic radii. An advantage of the method we have developed is the use of a solution of salts dissolved in ethylene glycol, which enables obtaining homogenous codoped NPs. The mechanism of the MSS reaction of $\text{Zn}_{(1-x-y)}\text{Mn}_x\text{Co}_y\text{O}$ NPs permits the substitution of Zn^{2+} ions with the optimum number of Mn^{2+} and Co^{2+} ions in the crystalline lattice of the ZnO being formed, depending on the precursor composition. The remaining quantity of Mn^{2+} and Co^{2+} , which has not been integrated into the crystalline lattice of ZnO, in turn, remains in the form of unreacted acetate salts dissolved in ethylene glycol [73]. In the sol-gel co-precipitation method, the codoping efficiency is 100% [102], which considerably reduces the costs of synthesis and chemical waste disposal. Nevertheless, thanks to the employment of ethylene glycol, a solvent with poor reducing properties, the MSS method prevents a change in the oxidation state of Mn^{2+} and Co^{2+} dopants [73,149,151], which considerably limits the possibility of formation of foreign phase inclusions. Another advantage of the MSS method is the use of a low synthesis temperature (190–220 °C) and a short synthesis time compared to other methods enumerated in Table 2, which prevents uncontrolled NPs growth, formation of NPs aggregates as a consequence of sintering, and formation of foreign phase inclusions during NPs growth.

Table 5. Results of the analysis of the chemical composition of $\text{Zn}_{(1-x-y)}\text{Mn}_x\text{Co}_y\text{O}$ samples.

Sample	Actual Dopant Content, mol %					
	EDS			ICP-OES		
	Zinc	Manganese	Cobalt	Zinc	Manganese	Cobalt
$\text{Zn}_{0.98}\text{Mn}_{0.01}\text{Co}_{0.01}\text{O}$	98.86	0.26	0.88	99.06	0.25	0.69
$\text{Zn}_{0.90}\text{Mn}_{0.05}\text{Co}_{0.05}\text{O}$	94.36	1.42	4.21	95.29	1.18	3.53
$\text{Zn}_{0.80}\text{Mn}_{0.10}\text{Co}_{0.10}\text{O}$	88.08	2.57	9.35	89.94	2.11	7.96
$\text{Zn}_{0.70}\text{Mn}_{0.15}\text{Co}_{0.15}\text{O}$	83.48	2.86	13.65	85.58	2.35	12.07

Table 6. Efficiency of ZnO codoping with Mn^{2+} and Co^{2+} ions.

Sample	Efficiency of Codoping Calculated Based on the Results of ICP-OES (%)	
	Manganese	Cobalt
$\text{Zn}_{0.98}\text{Mn}_{0.01}\text{Co}_{0.01}\text{O}$	25.00	69.00
$\text{Zn}_{0.90}\text{Mn}_{0.05}\text{Co}_{0.05}\text{O}$	23.60	70.60
$\text{Zn}_{0.80}\text{Mn}_{0.10}\text{Co}_{0.10}\text{O}$	21.10	79.60
$\text{Zn}_{0.70}\text{Mn}_{0.15}\text{Co}_{0.15}\text{O}$	15.67	80.47

It is generally known that ZnO codoping with Mn^{2+} and Co^{2+} ions causes a change in the optical properties and a reduction of the band gap width [103,105]. Figures 7 and 8 present a visual comparison of changes in the colours of $\text{Zn}_{(1-x-y)}\text{Mn}_x\text{Co}_y\text{O}$ samples depending on the content of dopants, while Table 7 summarises the results of the analysis of colours by the RGB and HSL colour models. ZnO codoping with Mn^{2+} and Co^{2+} ions resulted in a change of sample colour from light green to dark olive green. A similar change of $\text{Zn}_{(1-x-y)}\text{Mn}_x\text{Co}_y\text{O}$ powder colours is reported by Yin-Hua et al. [100]. The colour of the codoped ZnO is a resultant of the impact of the presence of two dopants in the ZnO crystalline lattice. Our earlier studies [149,150] showed that ZnO doped with Mn^{2+} ions changes colour from yellow to orange (Figure 7c) when the quantity of the Mn^{2+} dopant increases, while Co-doped ZnO NPs are green and the intensity of the colour depends on the content of the Co^{2+} dopant (Figure 7b). Based on the impact of a single dopant on the colour of ZnO, it can be inferred that the green colour of $\text{Zn}_{(1-x-y)}\text{Mn}_x\text{Co}_y\text{O}$ is attributed mainly to the presence of the Co^{2+} dopant. The modification of the colour of ZnO NPs through their codoping permits the application of $\text{Zn}_{(1-x-y)}\text{Mn}_x\text{Co}_y\text{O}$ nanopowders as colourful pigments. Obviously, when using $\text{Zn}_{(1-x-y)}\text{Mn}_x\text{Co}_y\text{O}$ NPs as pigments, their applications should be selected such that their potential toxicity is irrelevant.

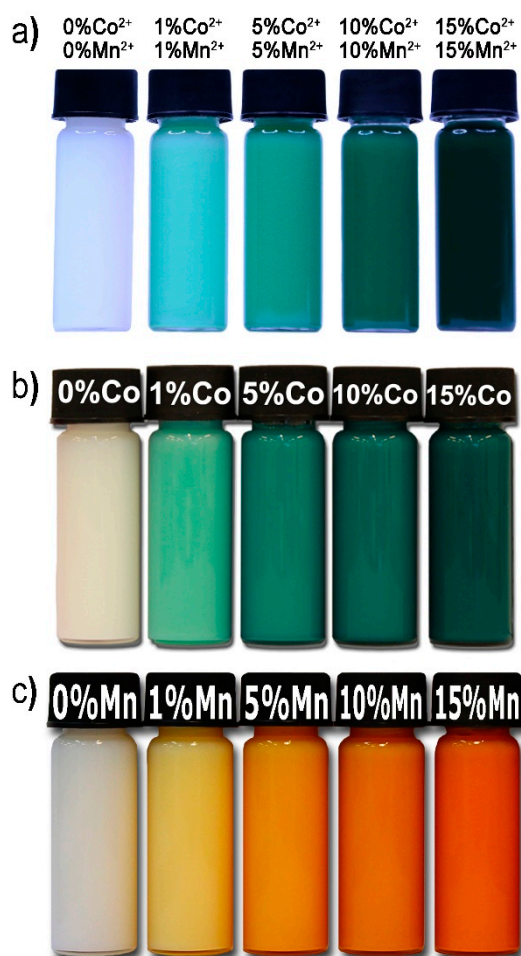


Figure 7. Photos of NP suspensions in ethylene glycol immediately after microwave solvothermal synthesis: (a) $Zn_{(1-x-y)}Mn_xCo_yO$, (b) $Zn_{(1-y)}Co_yO$ [150], (c) $Zn_{(1-x)}Mn_xO$ [149].

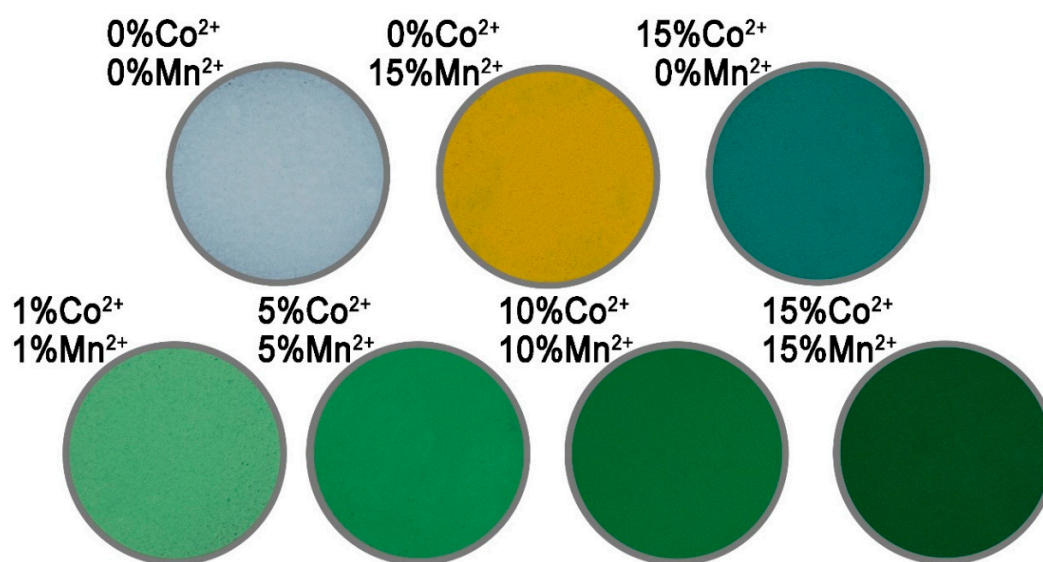


Figure 8. Photos of dry powders of $Zn_{(1-x-y)}Mn_xCo_yO$.

Table 7. Results of the colour analysis of dry NP samples (RGB and HSL colour model).

Sample	R (Red)	G (Green)	B (Blue)	H (Hue)	S (Saturation)	L (Luminance)
ZnO	1023	1023	1023	000	000	1000
Zn _{0.85} Co _{0.15} O	246	376	292	392	209	304
Zn _{0.85} Mn _{0.15} O	614	438	211	093	488	403
Zn _{0.98} Mn _{0.01} Co _{0.01} O	660	702	547	211	194	610
Zn _{0.90} Mn _{0.05} Co _{0.05} O	374	429	275	226	218	344
Zn _{0.80} Mn _{0.10} Co _{0.10} O	205	258	145	244	280	196
Zn _{0.70} Mn _{0.15} Co _{0.15} O	219	160	094	088	399	152

3.4. Density, Specific Surface Area and Size Distribution of NP

The obtained results are summarised in Table 8. The density of an undoped ZnO NP sample is 5.25 g/cm³ and is smaller than the value of 5.61 g/cm³ for the theoretical density of ZnO [164]. The difference between theoretical densities of the materials and real densities of these materials in the nano form is well known [140,151,165,166] and arises mainly from the imperfection of the real crystalline structure of nanomaterial surface, deviations from the stoichiometric composition, or the presence of hydroxides. With the theoretical density of CoO (6.45 g/cm³) and MnO (5.37 g/cm³) taken into consideration, it could be assumed that the density of the samples would increase in line with the growth of the dopant content in Zn_(1-x-y)Mn_xCo_yO. However, the density of Zn_(1-x-y)Mn_xCo_yO samples dropped from 5.25 g/cm³ to 5.06 g/cm³ in line with the increase in the dopant content, which could be explained by three causes:

- a different volume and packing of the unit cell of ZnO than in the case of MnO and CoO [6];
- lower atomic mass of the dopants (Co²⁺—≈58.93 u; Mn²⁺—≈54.94 u) in comparison to the substituted Zn²⁺ (≈65.38 u) atoms in the ZnO crystalline structure;
- increasing number of defects in the ZnO crystalline structure resulting from the growth of the content of Co²⁺ and Mn²⁺ dopants.

Table 8. Characteristics of the NP samples.

Sample	Specific Surface Area, a _s ± σ (m ² /g)	Skeleton Density, ρ _s ± σ (g/cm ³)	Average Particle Size from SSA BET, d ± σ (nm)	Average Crystallite Size from Nanopowder XRD Processor Demo, d ± σ (nm)	Average crystallite Size, Scherrer's Formula, d _a , d _c (nm)
ZnO	39.8 ± 0.1	5.25 ± 0.02	29 ± 1	22 ± 7	20a, 24c
Zn _{0.98} Mn _{0.01} Co _{0.01} O	46.4 ± 0.1	5.24 ± 0.02	24 ± 1	19 ± 6	16a, 18c
Zn _{0.90} Mn _{0.05} Co _{0.05} O	45.8 ± 0.1	5.23 ± 0.03	25 ± 1	22 ± 12	15a, 14c
Zn _{0.80} Mn _{0.10} Co _{0.10} O	50.6 ± 0.1	5.15 ± 0.03	23 ± 1	22 ± 13	14a, 11c
Zn _{0.70} Mn _{0.15} Co _{0.15} O	56.4 ± 0.1	5.06 ± 0.02	21 ± 1	22 ± 13	15a, 11c

d—diameter.

In line with the increase in the dopant content in Zn_(1-x-y)Mn_xCo_yO (Table 8), the specific surface area of the samples increased from 39.8 m²/g to 56.4 m²/g, while the average particle size calculated based on the specific surface area and density decreased from 29 nm to 21 nm. The average crystallite size calculated by the two methods fell within the range of standard deviations of these results. The ratio of the sizes of d_c i d_a crystallites proves a change in the asymmetry of the obtained Zn_(1-x-y)Mn_xCo_yO crystallites, and similar d_c/d_a values were obtained for Zn_(1-x)Mn_xO NPs depending on the dopant content [149]. The obtained crystallite size distribution of the Zn_(1-x-y)Mn_xCo_yO samples showed that the growth of the dopant content resulted in a wider distribution (Figure 9). The differences in the results between the average particle size and the average crystallite size might be caused by the adopted assumptions of the calculation methods employed [149,151,153,167], and the similar values of average particle and crystallite sizes prove that Zn_(1-x-y)Mn_xCo_yO particles are made of single crystallites.

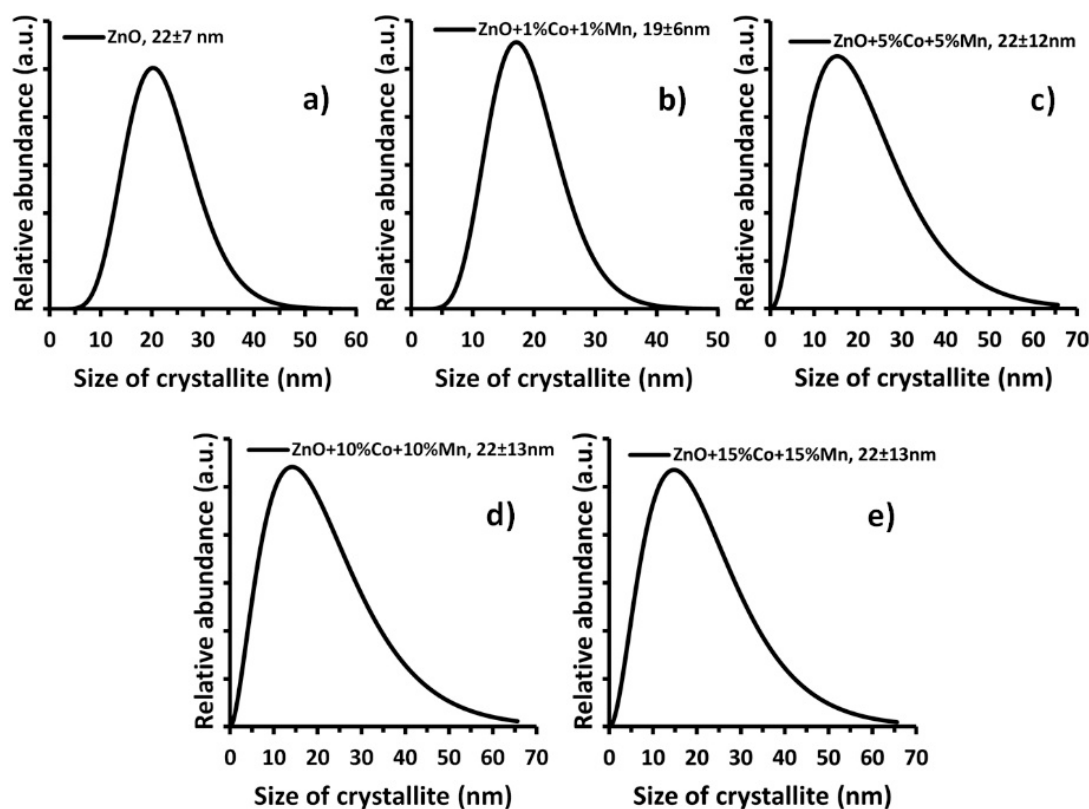


Figure 9. Crystallite size distribution of $Zn_{(1-x-y)}Mn_xCo_yO$ NPs: (a) ZnO , (b) $Zn_{0.98}Mn_{0.01}Co_{0.01}O$, (c) $Zn_{0.90}Mn_{0.05}Co_{0.05}O$, (d) $Zn_{0.80}Mn_{0.10}Co_{0.10}O$, and (e) $Zn_{0.70}Mn_{0.15}Co_{0.15}O$. Data obtained using Nanopowder XRD Processor Demo, pre- α -ver.0.0.8, © Pielaszek Research, <http://science24.com/xrd/>.

3.5. Magnetic Characterisation of the $Zn_{(1-x-y)}Mn_xCo_yO$ NPs

The representative magnetisation data are shown in Figure 10, where magnetisation as measured versus magnetic field is depicted at $T = 2$ K (a) and $T = 300$ K (b). Low-temperature data overall show typical paramagnetic behaviour: magnetisation increases monotonously in line with the increasing magnetic field and tends to saturate for the highest fields. For the samples with low concentrations of magnetic ions, saturation is nearly perfect, whereas for the highest concentrations magnetisation does not saturate in the applied field range. Such behaviour is typical for a paramagnetic system of localised magnetic moments of transition metals (TM) ions, coupled by an antiferromagnetic exchange interaction and was commonly observed for different. For lightly Mn^{2+}/Co^{2+} -doped samples this picture is confirmed by high-temperature data ($T = 300$ K), where magnetisation is a linear function of the magnetic field (cf. Figure 10b). On the other hand, high-temperature data for high Mn^{2+}/Co^{2+} concentrations reveal a different behaviour: magnetisation rises fast at low fields ($B < 1$ T), with a tendency to saturation, and then shows a linear field dependence (for $B > 1$ T). This suggests two components of the measured magnetisation: one purely paramagnetic, responsible for the linear field dependence and the second originating from ferro/ferrimagnetic phase arising during the growth process of the samples (e.g., Co_3O_4 , Mn_3O_4). We note that such a situation was widely encountered for DMS synthesised with TM concentration close to the solubility limits [168–170].

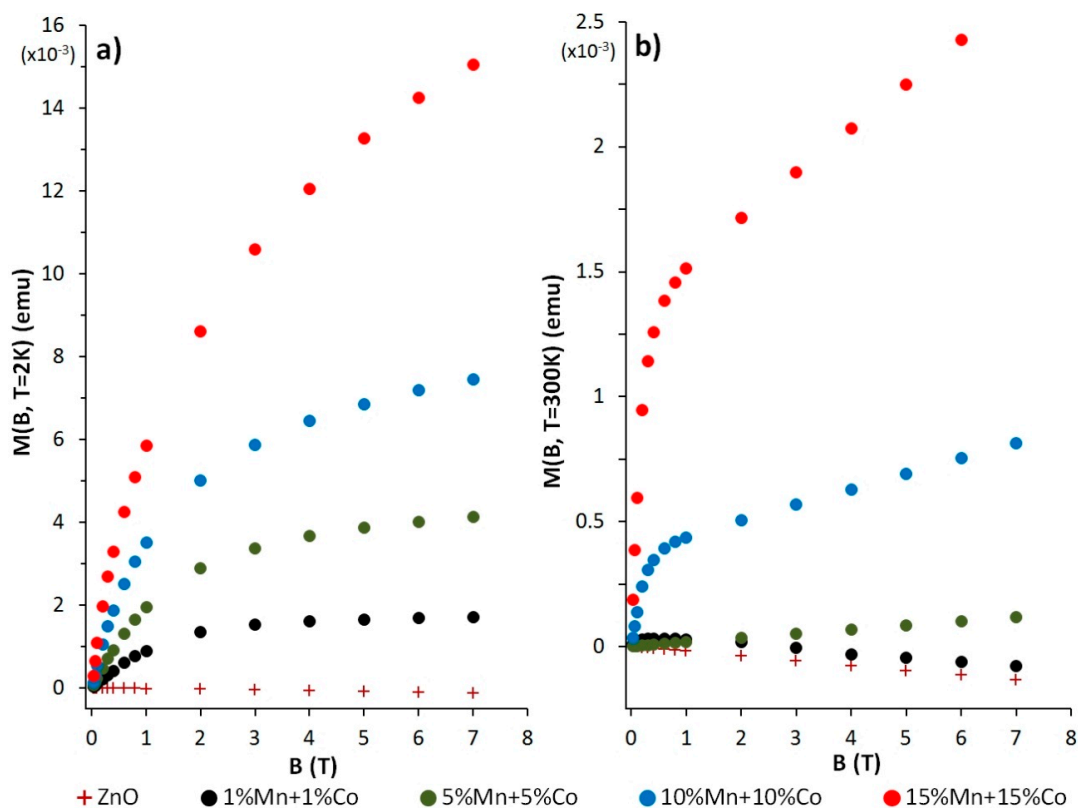


Figure 10. Measured magnetisation as a function of the magnetic field: (a) $\text{Zn}_{(1-x-y)}\text{Mn}_x\text{Co}_y\text{O}$ —temperature—2 K, (b) $\text{Zn}_{(1-x-y)}\text{Mn}_x\text{Co}_y\text{O}$ —temperature 300 K. Red full points— $\text{Zn}_{0.70}\text{Mn}_{0.15}\text{Co}_{0.15}\text{O}$, blue— $\text{Zn}_{0.80}\text{Mn}_{0.10}\text{Co}_{0.10}\text{O}$, green— $\text{Zn}_{0.90}\text{Mn}_{0.05}\text{Co}_{0.05}\text{O}$, black— $\text{Zn}_{0.98}\text{Mn}_{0.01}\text{Co}_{0.01}\text{O}$, brown crosses—pure ZnO.

Having the above in mind, the measured magnetic moment of each sample can be regarded as a sum of paramagnetic contributions of localised magnetic moments of Mn^{2+} or Co^{2+} ions, diamagnetic contributions of the NP lattice and the sample holder (parafilm wrapper, glue), as well as possible contributions of unintentional impurities/secondary phases. Therefore, the measured magnetic moment can be expressed in the form:

$$M_{\text{exp}}(B, T) = M_{\text{NP}}(B, T) + X_{\text{dia}} * B + C, \quad (4)$$

where $M_{\text{NP}}(B, T)$ is the total magnetisation of the magnetic moments of NPs, X_{dia} is the sum of diamagnetic susceptibility of NP, parafilm and glue (assumed to be temperature independent in the studied temperature range) and C represents the contribution from possible ferro/ferrimagnetic phases, as well as ferro/ferrimagnetic contributions of the ingredients used in the synthesis of the samples, parafilm and glue. As may be noticed from Figure 10b, the diamagnetic contribution for low concentrations of Mn/Co is sizeable and dominates the measured magnetic moment at high temperatures, e.g., at $T = 300\text{ K}$ the measured magnetic moment is diamagnetic. In such a case, precise values of X_{dia} and C for the sample in question are crucial. Instead of applying a standard way to evaluate X_{dia} , i.e., measuring the undoped sample (ZnO), it is proposed to eliminate $X_{\text{dia}} * B + C$ contributions by subtracting the high-temperature magnetic moment (where the paramagnetic contribution of Mn/Co magnetic moments is largely quenched) from the low-temperature one. Assuming that X_{dia} and C are temperature-independent (which is true to a large extent), the following is obtained:

$$M_{\text{exp}}(B, T = 2\text{ K}) - M_{\text{exp}}(B, T = 300\text{ K}) = M_{\text{NP}}(B, T = 2\text{ K}) - M_{\text{NP}}(B, T = 300\text{ K}), \quad (5)$$

Given the previous results for Mn^{2+} - and Co^{2+} -base DMS, $M_{\text{NP}}(B, T)$ can be assumed in the following form:

$$M_{\text{NP}}(B, T) = A g \mu_{\text{B}} S B_{\text{S}}(B, T), \quad (6)$$

where $B_{\text{S}}(B, T)$ is the Brillouin function for spin $S = 5/2$ (Mn^{2+}) or $S = 3/2$ (Co^{2+}), $g = 2.00$ is the g-factor, μ_{B} is the Bohr magneton and A is the number of spins (magnetic moments) in the sample. A possible interaction between spins can be taken into account by assuming effective temperature $T_{\text{eff}} = T - T_0$, instead of experimental temperature T [171,172]. We recall that $T_0 < 0$ corresponds to antiferromagnetic (AFM) interactions, while $T_0 > 0$ means ferromagnetic (FM) interactions.

In order to demonstrate how the proposed method works, we start with NPs doped only with one type of ions, i.e., Mn^{2+} or Co^{2+} . The results concerning the characterisation of $\text{Zn}_{0.99}\text{Mn}_{0.01}\text{O}$, $\text{Zn}_{0.85}\text{Mn}_{0.15}\text{O}$, $\text{Zn}_{0.99}\text{Co}_{0.01}\text{O}$ and $\text{Zn}_{0.85}\text{Co}_{0.15}\text{O}$ samples are included in the Supplementary Materials Figure 11a shows $M_{\text{exp}}(B, T = 2 \text{ K}) - M_{\text{exp}}(B, T = 300 \text{ K})$, as well as the fit with Equations (5) and (6), where A was the only adjustable parameter (spin $S = 5/2$ and $T_0 = 0$ were fixed).

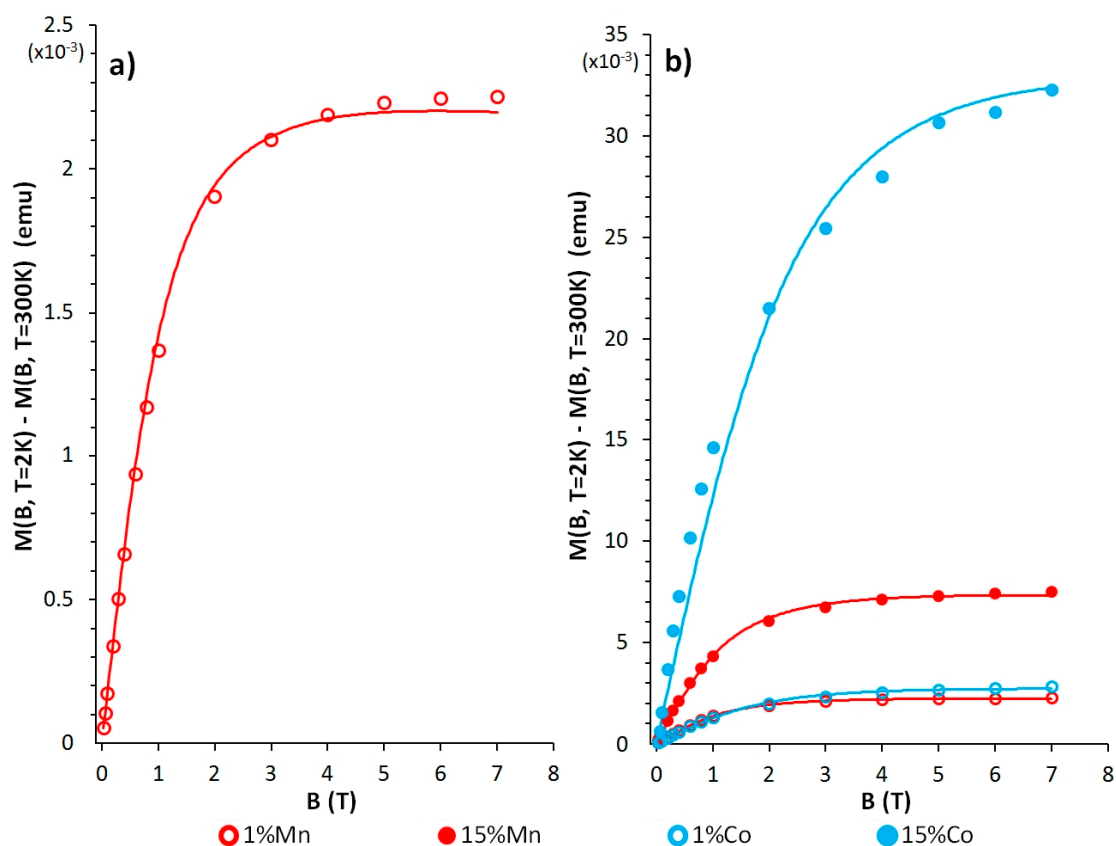


Figure 11. Magnetisation difference $M_{\text{exp}}(B, T = 2 \text{ K}) - M_{\text{exp}}(B, T = 300 \text{ K})$ as a function of the magnetic field for: (a) $\text{Zn}_{0.99}\text{Mn}_{0.01}\text{O}$, solid line: fit with Equations (5) and (6); T_0 was set to 0 K; (b) $\text{Zn}_{0.99}\text{Mn}_{0.01}\text{O}$ and $\text{Zn}_{0.85}\text{Mn}_{0.15}\text{O}$ (red), solid lines: fits with Equations (5) and (6), with $S = 5/2$ and T_0 as an adjustable parameter ($T_0 = -0.17 \text{ K}$ for $\text{Zn}_{0.99}\text{Mn}_{0.01}\text{O}$ and $T_0 = -0.29 \text{ K}$ for $\text{Zn}_{0.85}\text{Mn}_{0.15}\text{O}$ sample), $\text{Zn}_{0.99}\text{Co}_{0.01}\text{O}$ and $\text{Zn}_{0.85}\text{Co}_{0.15}\text{O}$ (blue), solid lines: fits with Equations (5) and (6), with $S = 3/2$ and T_0 as an adjustable parameter ($T_0 = -0.24 \text{ K}$ for $\text{Zn}_{0.99}\text{Co}_{0.01}\text{O}$ and $T_0 = -0.95 \text{ K}$ for $\text{Zn}_{0.85}\text{Co}_{0.15}\text{O}$ sample).

The slower saturation of magnetisation $M_{\text{NP}}(B, T)$ than the Brillouin function reflects AFM interaction between Mn^{2+} ions, which is expected for the system with about 1% of Mn^{2+} ions [172]. As mentioned above, this effect can be taken into account by introducing effective temperature $T_{\text{eff}} = T - T_0$ and considering T_0 as an adjustable parameter. Figure 11b shows $M_{\text{exp}}(B, T = 2 \text{ K}) - M_{\text{exp}}(B, T = 300 \text{ K})$, as well as the fits with Equations (5) and (6), where A and T_0 are adjustable parameters (spin $S = 5/2$ or $S = 3/2$ are fixed).

Satisfactory matching was obtained for all the samples. Effective temperatures T_0 are all negative, indicating AFM exchange interactions between Mn^{2+} and Co^{2+} ions, as expected [171,172].

For the samples codoped with both Mn^{2+} and Co^{2+} the following function was used:

$$M_{NP}(B, T) = A_{Mn} g \mu_B S_{Mn} B_S(B, T_{eff}) + A_{Co} g \mu_B S_{Co} B_S(B, T_{eff}), \quad (7)$$

where A_{Mn} (A_{Co}) corresponds to number of Mn^{2+} (Co^{2+}) ions, $S_{Mn} = 5/2$, $S_{Co} = 3/2$. In order to avoid a large number of fitting parameters only one effective temperature was used, which means that T_0 is a common parameter for all interactions in the NP, i.e., Mn^{2+} - Mn^{2+} , Co^{2+} - Co^{2+} and Mn^{2+} - Co^{2+} .

The results of the fittings are shown in Figure 12. For all the samples T_0 is negative, suggesting preferred antiferromagnetic interactions between Mn and Co ions.

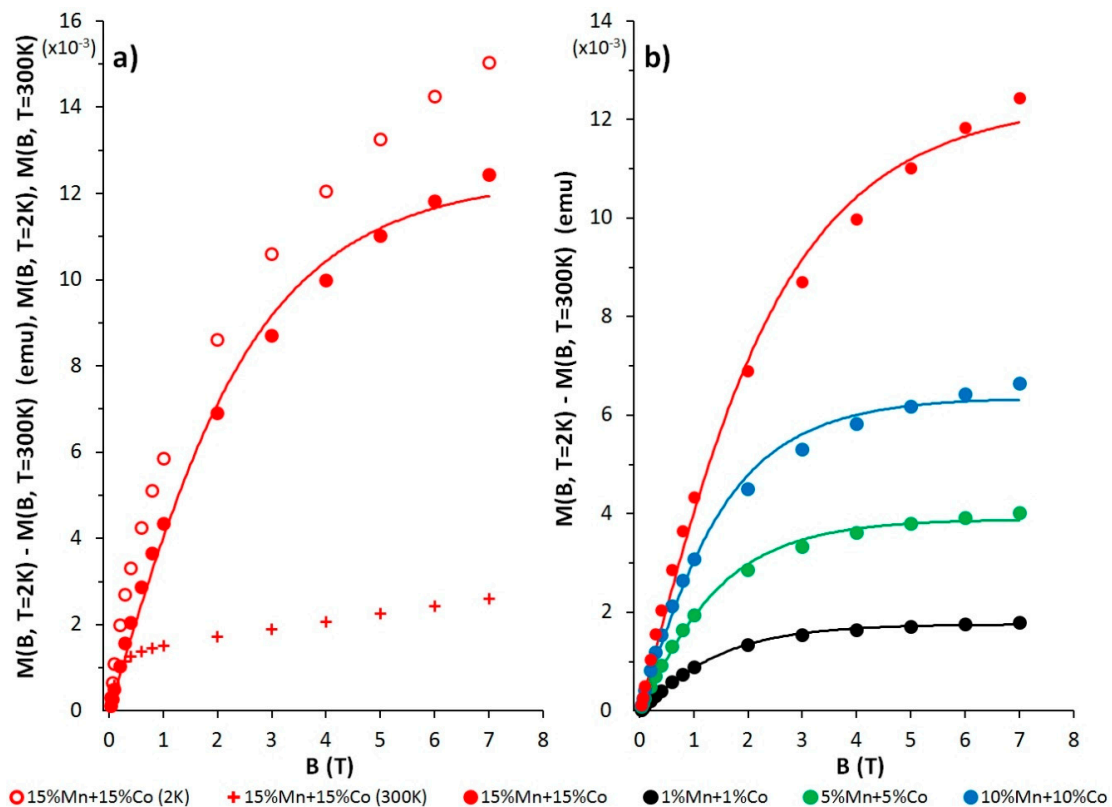


Figure 12. Magnetisation $M_{exp}(B, T = 2\text{ K}) - M_{exp}(B, T = 300\text{ K})$ of codoped ZnO NPs with Mn^{2+} and Co^{2+} versus magnetic field: (a) $Zn_{0.70}Mn_{0.15}Co_{0.15}O$ empty points— $M_{exp}(B, T = 2\text{ K})$, crosses— $M_{exp}(B, T = 300\text{ K})$, full points $M_{exp}(B, T = 2\text{ K}) - M_{exp}(B, T = 300\text{ K})$, solid line—fit with Equation (7); (b) $M_{exp}(B, T = 2\text{ K}) - M_{exp}(B, T = 300\text{ K})$ for $Zn_{0.70}Mn_{0.15}Co_{0.15}O$ (red), $Zn_{0.80}Mn_{0.10}Co_{0.10}O$ (blue), $Zn_{0.90}Mn_{0.05}Co_{0.05}O$ (green), $Zn_{0.98}Mn_{0.01}Co_{0.01}O$ (black). Solid lines—fits with Equation (7), where ratio A_{Mn}/A_{Co} was kept as resulting from Table 5. The resulting T_0 are the following: $T_0 = -1.78\text{ K}$ for $Zn_{0.70}Mn_{0.15}Co_{0.15}O$ (red), $T_0 = -0.42\text{ K}$ for $Zn_{0.80}Mn_{0.10}Co_{0.10}O$ (blue), $T_0 = -0.37\text{ K}$ for $Zn_{0.90}Mn_{0.05}Co_{0.05}O$ (green), $T_0 = -0.35\text{ K}$ for $Zn_{0.98}Mn_{0.01}Co_{0.01}O$ (black).

To summarise the magnetic properties, it can be stated that the discussed NP samples can be generally described as the systems of localised magnetic moments arising from Mn^{2+} or Co^{2+} d-shell electrons located at Zn^{2+} lattice sites. The paramagnetic properties of these systems can be reasonably well described by the effective Brillouin function, with an indication of AFM exchange interactions between Mn^{2+} or Co^{2+} ions. Moreover, for the $Zn_{0.70}Mn_{0.15}Co_{0.15}O$ samples with the highest TM ions concentrations, an additional ferromagnetic-type magnetic phase is observed, most probably originating from crystalline phases other than $Zn_{(1-x-y)}Mn_xCo_yO$.

The $\text{Zn}_{0.70}\text{Mn}_{0.15}\text{Co}_{0.15}\text{O}$ NP sample is a good example, confirming our earlier research results [73]. Namely, we stated that if a ZnO sample displays ferromagnetic properties, this may be caused by the presence of a foreign phase or a change in the dopant oxidation state. XRD tests did not indicate the presence of a foreign phase in the $\text{Zn}_{0.70}\text{Mn}_{0.15}\text{Co}_{0.15}\text{O}$ NP sample, but the SEM images (Figure 3a) show a small quantity of a lamellar structure, which probably is a foreign phase.

4. Conclusions

ZnO nanoparticles strongly codoped with Mn^{2+} and Co^{2+} ions up to the nominal content of 15 mol % were obtained for the first time by means of the microwave solvothermal synthesis method. The reaction precursors were solutions of zinc acetate, manganese acetate (II), and cobalt acetate (II) dissolved in ethylene glycol. No other phases were detected by means of X-ray diffraction in all obtained samples. The actual Mn^{2+} and Co^{2+} ions dopant content ranged from 15.67% to 25.00% and from 69.00% and 80.47% of the nominal one, respectively. The colour of $\text{Zn}_{(1-x-y)}\text{Mn}_x\text{Co}_y\text{O}$ NP samples changed in line with the dopants value from white (undoped ZnO), through light green ($\text{Zn}_{0.98}\text{Mn}_{0.01}\text{Co}_{0.01}\text{O}$), to dark olive green ($\text{Zn}_{0.70}\text{Co}_{0.15}\text{Mn}_{0.15}\text{O}$). The obtained results of the chemical composition, the increase in the crystalline lattice parameters, and the changes of colours confirmed the successful codoping of ZnO NPs with Mn^{2+} and Co^{2+} ions. $\text{Zn}_{(1-x-y)}\text{Mn}_x\text{Co}_y\text{O}$ powders are composed of homogenous spherical NPs, which, depending on the dopants content, form aggregates resembling a “cauliflower” structure. Only in the $\text{Zn}_{0.7}\text{Mn}_{0.15}\text{Co}_{0.15}\text{O}$ sample was a small quantity of an unidentified lamellar structure observed. The growth of the dopant content from 0% ($x = y$) to 15% ($x = y$) in $\text{Zn}_{(1-x-y)}\text{Mn}_x\text{Co}_y\text{O}$ NPs caused an increase in the specific surface area from $39.8 \text{ m}^2/\text{g}$ to $56.4 \text{ m}^2/\text{g}$; a decrease in density from $5.25 \text{ g}/\text{cm}^3$ to $5.06 \text{ g}/\text{cm}^3$; and a decrease in the average NPs size from 29 nm to 21 nm.

The magnetic properties of the nanoparticles can be described as systems of localised magnetic moments arising from Mn^{2+} or Co^{2+} d-shell electrons located at Zn^{2+} lattice sites. The paramagnetic properties of these nanoparticles are described by the effective Brillouin function, with an indication of antiferromagnetic exchange interactions between Mn^{2+} or Co^{2+} ions. For the $\text{Zn}_{0.70}\text{Mn}_{0.15}\text{Co}_{0.15}\text{O}$ samples with the highest ion concentrations, an additional, ferromagnetic-type magnetic phase is observed.

The achieved results confirm the numerous advantages of the microwave solvothermal synthesis in obtaining codoped ZnO NPs.

Supplementary Materials: The following are available online at <http://www.mdpi.com/2073-4352/8/11/410/s1>.

Author Contributions: J.W., W.L., M.O. and J.S. conceived and designed the experiments; J.W., M.O. and S.G. performed the experiments; J.W., M.O., J.S., T.C., S.G., A.M., A.T. and W.L. analysed the data; J.W., J.S., A.T. and W.L. contributed reagents/materials/analysis tools; J.W., M.O., J.S., A.T. and W.L. wrote the paper.

Funding: The work was supported by the Institute of High Pressure Physics, the Polish Academy of Sciences.

Acknowledgments: The research was carried out using equipment funded by the CePT project, reference: POIG.02.02.00-14-024/08, financed by the European Regional development Fund within the Operational Programme “Innovative Economy” for 2007–2013. The authors would also like to thank Magdalena Grochowska (Faculty of Physics, University of Warsaw), Jan Mizeracki (Institute of High Pressure Physics of the Polish Academy of Sciences) and Roman Mukhovskiy.

Conflicts of Interest: The authors declare no conflict of interest.

References

1. Fortunato, E.; Gonçalves, A.; Pimentel, A.; Barquinha, P.; Gonçalves, G.; Pereira, L.; Ferreira, I.; Martins, R. Zinc oxide, a multifunctional material: From material to device applications. *Appl. Phys. A* **2009**, *96*, 197–205. [[CrossRef](#)]
2. Ali, A.; Phull, A.R.; Zia, M. Elemental Zinc to Zinc nanoparticles: Is ZnO NPs crucial for life? Synthesis, toxicological and environmental concerns. *Nanotechnol. Rev.* **2018**, *7*, 413–441. [[CrossRef](#)]

3. Ashrafi, A.; Jagadish, C. Review of zincblende ZnO: Stability of metastable ZnO phases. *J. Appl. Phys.* **2007**, *102*, 071101. [[CrossRef](#)]
4. Ozgur, U.; Alivov, Y.I.; Liu, C.; Teke, A.; Reshchikov, M.A.; Dogan, S.; Avrutin, V.; Cho, S.J.; Morkoc, H. A comprehensive review of ZnO materials and devices. *J. Appl. Phys.* **2005**, *98*, 041301. [[CrossRef](#)]
5. Jagadish, C.; Pearton, S. *Zinc Oxide Bulk, Thin Films and Nanostructures*, 1st ed.; Elsevier: Oxford, UK, 2006; ISBN 978-0-08-044722-3.
6. Morkoç, H.; Özgür, Ü. *Zinc Oxide: Fundamentals, Materials and Device Technology*, 1st ed.; WILEY-VCH: Weinheim, Germany, 2009; ISBN 978-3-527-40813-9.
7. Ozgur, U.; Hofstetter, D.; Morkoc, H. ZnO devices and applications: A review of current status and future prospects. *Proc. IEEE* **2010**, *98*, 1255–1268. [[CrossRef](#)]
8. Litton, C.W.; Reynolds, D.C.; Collins, T.C. *Zinc Oxide Materials for Electronic and Optoelectronic Device Applications*, 1st ed.; John Wiley & Sons, Ltd.: Chichester, UK, 2011; ISBN 9780470519714.
9. Willander, M. *Zinc Oxide Nanostructures: Advances and Applications*, 1st ed.; Pan Stanford: New York, NY, USA, 2014; ISBN 9789814411332.
10. Djurišić, A.B.; Ng, A.M.C.; Chen, X.Y. ZnO Nanostructures for Optoelectronics: Material Properties and Device Applications. *Prog. Quantum Electron.* **2010**, *34*, 191–259. [[CrossRef](#)]
11. Oprea, O.; Andronescu, E.; Fikai, D.; Fikai, A.; Oktar, F.N.; Yetmez, M. ZnO Applications and Challenges. *Curr. Org. Chem.* **2014**, *18*, 192–203. [[CrossRef](#)]
12. Martínez-Carmona, M.; Gun'ko, Y.; Vallet-Regí, M. ZnO Nanostructures for Drug Delivery and Theranostic Applications. *Nanomaterials* **2018**, *8*, 268. [[CrossRef](#)] [[PubMed](#)]
13. Jiang, J.; Pi, J.; Cai, J. The Advancing of Zinc Oxide Nanoparticles for Biomedical Applications. *Bioinorg. Chem. Appl.* **2018**, *2018*, 1062562. [[CrossRef](#)] [[PubMed](#)]
14. Sirelkhatim, A.; Mahmud, S.; Seeni, S.; Kaus, A.S.N.; Ann, L.C.; Bakhori, S.K.M.; Hasan, H.; Mohamad, D. Review on Zinc Oxide Nanoparticles: Antibacterial Activity and Toxicity Mechanism. *Nano-Micro Lett.* **2015**, *7*, 219–242. [[CrossRef](#)]
15. Zhang, Y.; Nayak, T.R.; Hong, H.; Cai, W. Biomedical Applications of Zinc Oxide Nanomaterials. *Curr. Mol. Med.* **2013**, *13*, 1633–1645. [[CrossRef](#)] [[PubMed](#)]
16. Sruthi, S.; Mohanan, P.V. Engineered Zinc Oxide Nanoparticles; Biological Interactions at the Organ Level. *Curr. Med. Chem.* **2016**, *23*, 4057–4068. [[CrossRef](#)] [[PubMed](#)]
17. Kalpana, V.N.; Devi Rajeswari, V. A Review on Green Synthesis, Biomedical Applications, and Toxicity Studies of ZnO NPs. *Bioinorg. Chem. Appl.* **2018**, *2018*, 3569758. [[CrossRef](#)] [[PubMed](#)]
18. Cierech, M.; Kolenda, A.; Grudniak, A.M.; Wojnarowicz, J.; Woźniak, B.; Gołaś, M.; Swoboda-Kopeć, E.; Łojkowski, W.; Mierzwińska-Nastalska, E. Significance of polymethylmethacrylate (PMMA) modification by zinc oxide nanoparticles for fungal biofilm formation. *Int. J. Pharm.* **2016**, *510*, 323–335. [[CrossRef](#)] [[PubMed](#)]
19. Cierech, M.; Wojnarowicz, J.; Szmigiel, D.; Bączkowski, B.; Grudniak, A.; Wolska, K.; Łojkowski, W.; Mierzwińska-Nastalska, E. Preparation and characterization of ZnO-PMMA resin nanocomposites for denture bases. *Acta Bioeng. Biomech.* **2016**, *18*, 31–41. [[CrossRef](#)] [[PubMed](#)]
20. Cierech, M.; Osica, I.; Kolenda, A.; Wojnarowicz, J.; Szmigiel, D.; Łojkowski, W.; Kurzydłowski, K.; Ariga, K.; Mierzwińska-Nastalska, E. Mechanical and Physicochemical Properties of Newly Formed ZnO-PMMA Nanocomposites for Denture Bases. *Nanomaterials* **2018**, *8*, 305. [[CrossRef](#)] [[PubMed](#)]
21. Paszek, E.; Czyz, J.; Woźniacka, O.; Jakubiak, D.; Wojnarowicz, J.; Łojkowski, W.; Stępień, E. Zinc oxide nanoparticles impair the integrity of human umbilical vein endothelial cell monolayer in vitro. *J. Biomed. Nanotechnol.* **2012**, *8*, 957–967. [[CrossRef](#)] [[PubMed](#)]
22. Pokrowiecki, R.; Pałka, K.; Mielczarek, A. Nanomaterials in dentistry: A cornerstone or a black box? *Nanomedicine* **2018**, *13*, 639–667. [[CrossRef](#)] [[PubMed](#)]
23. Jamalullail, N.; Mohamad, I.S.; Norizan, M.N.; Mahmed, N.; Taib, B.N. Recent improvements on TiO₂ and ZnO nanostructure photoanode for dye sensitized solar cells: A brief review. *EPJ Web Conf.* **2017**, *162*, 01045. [[CrossRef](#)]
24. Luo, J.; Wang, Y.; Zhang, Q. Progress in perovskite solar cells based on ZnO nanostructures. *Sol. Energy* **2018**, *163*, 289–306. [[CrossRef](#)]
25. Melo, A.H.N.; Macêdo, M.A. Permanent Data Storage in ZnO Thin Films by Filamentary Resistive Switching. *PLoS ONE* **2016**, *11*, e0168515. [[CrossRef](#)] [[PubMed](#)]

26. Omelchenko, M.M.; Wojnarowicz, J.; Salamonczyk, M.; Lojkowski, W. Lyotropic liquid crystal based on zinc oxide nanoparticles obtained by microwave solvothermal synthesis. *Mater. Chem. Phys.* **2017**, *192*, 383–391. [[CrossRef](#)]
27. Salzano de Luna, M.; Galizia, M.; Wojnarowicz, J.; Rosa, R.; Lojkowski, W.; Acierno, D.; Filippone, G.; Leonelli, C. Dispersing hydrophilic nanoparticles in hydrophobic polymers: HDPE/ZnO nanocomposites by a novel template-based approach. *Express Polym. Lett.* **2014**, *8*, 362–372. [[CrossRef](#)]
28. Huang, J.; Huang, G.; An, C.; He, Y.; Yao, Y.; Zhang, P.; Shen, J. Performance of ceramic disk filter coated with nano ZnO for removing Escherichia coli from water in small rural and remote communities of developing regions. *Environ. Pollut.* **2018**, *238*, 52–62. [[CrossRef](#)] [[PubMed](#)]
29. Ong, C.B.; Ng, L.Y.; Mohammad, A.W. A review of ZnO nanoparticles as solar photocatalysts: Synthesis, mechanisms and applications. *Renew. Sustain. Energy Rev.* **2018**, *81*, 536–551. [[CrossRef](#)]
30. Hamid, S.B.A.; Teh, S.J.; Lai, C.W. Photocatalytic Water Oxidation on ZnO: A Review. *Catalysts* **2017**, *7*, 93. [[CrossRef](#)]
31. Tudose, I.V.; Suche, M. ZnO for photocatalytic air purification applications. *IOP Conf. Ser. Mater. Sci. Eng.* **2016**, *133*, 012040. [[CrossRef](#)]
32. Djurišić, A.B.; Chen, X.; Leung, Y.H.; Ng, A.M.C. ZnO nanostructures: Growth, properties and applications. *J. Mater. Chem.* **2012**, *22*, 6526–6535. [[CrossRef](#)]
33. Chaudhary, S.; Umar, A. ZnO Nanostructures and Their Sensing Applications: A Review. *Nanosci. Nanotechnol. Lett.* **2017**, *9*, 1787–1826. [[CrossRef](#)]
34. Woźniak, B.; Dąbrowska, S.; Wojnarowicz, J.; Chudoba, T.; Łojkowski, W. Content available remote Coating synthetic materials with zinc oxide nanoparticles acting as a UV filter. *Glass Ceram.* **2017**, *3*, 15–17.
35. Fu, Y.; Fu, W.; Liu, Y.; Zhang, G.; Liu, Y.; Yu, H. Comparison of ZnO nanorod array coatings on wood and their UV prevention effects obtained by microwave-assisted hydrothermal and conventional hydrothermal synthesis. *Holzforschung* **2015**, *69*, 1009–1014. [[CrossRef](#)]
36. Wallenhorst, L.; Gurău, L.; Gellerich, A.; Militz, H.; Ohms, G.; Viöl, W. UV-blocking properties of Zn/ZnO coatings on wood deposited by cold plasma spraying at atmospheric pressure. *Appl. Surf. Sci.* **2018**, *434*, 1183–1192. [[CrossRef](#)]
37. Sabir, S.; Arshad, M.; Chaudhari, K.C. Zinc Oxide Nanoparticles for Revolutionizing Agriculture: Synthesis and Applications. *Sci. World J.* **2014**, *2014*, 925494. [[CrossRef](#)] [[PubMed](#)]
38. Singh, A.; Singh, N.B.; Afzal, S.; Singh, T.; Hussain, I. Zinc oxide nanoparticles: A review of their biological synthesis, antimicrobial activity, uptake, translocation and biotransformation in plants. *J. Mater. Sci.* **2018**, *53*, 185–201. [[CrossRef](#)]
39. Pearton, S.J.; Norton, D.P.; Heo, Y.W.; Tien, L.C.; Ivill, M.P.; Li, Y.; Kang, B.S.; Ren, F.; Kelly, J.; Hebard, A.F. ZnO spintronics and nanowire devices. *J. Electron. Mater.* **2006**, *35*, 862–868. [[CrossRef](#)]
40. Lu, J.W.; Chen, E.; Kabir, M.; Stan, M.R.; Wolf, S.A. Spintronics technology: Past, present and future. *Int. Mater. Rev.* **2016**, *61*, 456–472. [[CrossRef](#)]
41. Awschalom, D.D.; Flatté, M.E. Challenges for semiconductor spintronics. *Nat. Phys.* **2007**, *3*, 153–159. [[CrossRef](#)]
42. Dietl, T.; Ohno, H.; Matsukura, M.; Cibert, J.; Ferrand, D. Zener Model Description of Ferromagnetism in Zinc-Blende Magnetic Semiconductors. *Science* **2000**, *287*, 1019–2000. [[CrossRef](#)] [[PubMed](#)]
43. Sato, K.; Katayama-Yosida, H. First principles materials design for semiconductor spintronics. *Semicond. Sci. Technol.* **2002**, *17*, 367–376. [[CrossRef](#)]
44. Mustaqima, M.; Liu, C. ZnO-based nanostructures for diluted magnetic semiconductor. *Turk. J. Phys.* **2014**, *38*, 429–441. [[CrossRef](#)]
45. Djerdj, I.; Jagličić, Z.; Arcon, D.; Niederberger, M. Co-Doped ZnO nanoparticles: Minireview. *Nanoscale* **2010**, *2*, 1096–1104. [[CrossRef](#)] [[PubMed](#)]
46. Yang, Z. A perspective of recent progress in ZnO diluted magnetic semiconductors. *Appl. Phys. A* **2013**, *112*, 241–254. [[CrossRef](#)]
47. Liu, C.; Yun, F.; Morkoç, H. Ferromagnetism of ZnO and GaN: A Review. *J. Mater. Sci. Mater. Electron.* **2005**, *16*, 555–597. [[CrossRef](#)]
48. Naeem, M.; Hasanain, S.K.; Kobayashi, M.; Ishida, Y.; Fujimori, A.; Buzby, S.; Shah, S.I. Effect of reducing atmosphere on the magnetism of Zn_{1-x}Co_xO (0 ≤ x ≤ 0.10) nanoparticles. *Nanotechnology* **2006**, *17*, 2675. [[CrossRef](#)] [[PubMed](#)]

49. Yang, L.W.; Wu, X.L.; Qiu, T. Synthesis and magnetic properties of $Zn_{1-x}Co_xO$ nanorods. *J. Appl. Phys.* **2006**, *99*, 074303. [[CrossRef](#)]
50. Sharrouf, M.; Awad, R.; Marhaba, S.; El-Said Bakeer, D. Structural, Optical and Room Temperature Magnetic Study of Mn-Doped ZnO Nanoparticles. *Nano* **2016**, *11*, 1650042. [[CrossRef](#)]
51. Fu, J.; Pen, X.; Yan, S.; Gong, Y.; Tan, Y.; Liang, R.; Du, R.; Xing, X.; Mo, G.; Chen, Z.; et al. Synthesis and structural characterization of ZnO doped with Co. *J. Alloys Compd.* **2013**, *558*, 212–221. [[CrossRef](#)]
52. Omri, K.; El Ghouli, J.; Lemine, O.M.; Bououdina, M.; Zhang, B.; El Mir, L. Magnetic and optical properties of manganese doped ZnO nanoparticles synthesized by sol–gel technique. *Superlattices Microstruct.* **2013**, *60*, 139–147. [[CrossRef](#)]
53. Sharma, V.K.; Najim, M.; Srivastava, A.K.; Varma, G.D. Structural and magnetic studies on transition metal (Mn, Co) doped ZnO nanoparticles. *J. Magn. Magn. Mater.* **2012**, *324*, 683–689. [[CrossRef](#)]
54. Blasco, J.; Bartolomé, F.; García, L.M.; García, J.J. Extrinsic origin of ferromagnetism in doped ZnO. *J. Mater. Chem.* **2006**, *16*, 2282–2288. [[CrossRef](#)]
55. Xu, X.; Cao, C. Hydrothermal synthesis of Co-doped ZnO flakes with room temperature ferromagnetism. *J. Alloys Compd.* **2010**, *501*, 265–268. [[CrossRef](#)]
56. Mandal, S.K.; Das, A.K.; Natha, T.K. Microstructural and magnetic properties of ZnO:TM (TM = Co, Mn) diluted magnetic semiconducting nanoparticles. *J. Appl. Phys.* **2006**, *100*, 104315. [[CrossRef](#)]
57. Kuryliszyn-Kudelska, I.; Dobrowolski, W.D.; Kilański, Ł.; Hadžić, B.; Romčević, N.; Sibera, D.; Narkiewicz, U.; Dziawa, P. Magnetic properties of nanocrystalline ZnO doped with MnO and CoO. *J. Phys. Conf. Ser.* **2010**, *200*, 072058. [[CrossRef](#)]
58. Kuryliszyn-Kudelska, I.; Dobrowolski, W.; Arciszewska, M.; Romčević, N.; Romčević, M.; Hadžić, B.; Sibera, D.; Narkiewicz, U.; Lojkowski, W. Transition metals in ZnO nanocrystals: Magnetic and structural properties. *Sci. Sinter.* **2013**, *45*, 31–48. [[CrossRef](#)]
59. Kuryliszyn-Kudelska, I.; Dobrowolski, W.; Arciszewska, M.; Romčević, N.; Romčević, M.; Hadžić, B.; Sibera, D.; Narkiewicz, U. Superparamagnetic and ferrimagnetic behavior of nanocrystalline ZnO(MnO). *Phys. E Low-Dimens. Syst. Nanostruct.* **2018**, *98*, 10–16. [[CrossRef](#)]
60. Żolnierkiewicz, G.; Typek, J.; Guskos, N.; Narkiewicz, U.; Sibera, D. Magnetic resonance study of nanocrystalline 0.10MnO/0.90ZnO. *Cent. Eur. J. Phys.* **2013**, *11*, 226–230. [[CrossRef](#)]
61. Li, J.H.; Shen, D.Z.; Zhang, J.Y.; Zhao, D.X.; Li, B.S.; Lu, Y.M.; Liu, Y.C.; Fan, X.W. Magnetism origin of Mn-doped ZnO nanoclusters. *J. Magn. Magn. Mater.* **2006**, *302*, 118–121. [[CrossRef](#)]
62. Samanta, K.; Bhattacharya, P.; Katiyar, R.S.; Iwamoto, W.; Pagliuso, P.G.; Rettori, C. Raman scattering studies in dilute magnetic semiconductor $Zn_{1-x}Co_xO$. *Phys. Rev. B* **2006**, *73*, 245213. [[CrossRef](#)]
63. Kuryliszyn-Kudelska, I.; Hadžić, B.; Sibera, D.; Romčević, M.; Romčević, N.; Narkiewicz, U.; Lojkowski, W.; Arciszewska, M.; Dobrowolski, W. Magnetic properties of ZnO(Co) nanocrystals. *J. Alloys Compd.* **2013**, *561*, 247–251. [[CrossRef](#)]
64. Typek, J.; Guskos, N.; Zolnierkiewicz, G.; Sibera, D.; Narkiewicz, U. Magnetic resonance study of Co-doped ZnO nanomaterials: A case of high doping. *Rev. Adv. Mater. Sci.* **2017**, *50*, 76–87.
65. Birajdar, S.D.; Alange, R.C.; More, S.D.; Murumkar, V.D.; Jadhav, K.M. Sol-gel Auto Combustion Synthesis, Structural and Magnetic Properties of Mn doped ZnO Nanoparticles. *Procedia Manuf.* **2018**, *20*, 174–180. [[CrossRef](#)]
66. Luo, X.; Lee, W.T.; Xing, G.; Bao, N.; Yonis, A.; Chu, D.; Lee, J.; Ding, J.; Li, S.; Yi, J. Ferromagnetic ordering in Mn-doped ZnO nanoparticles. *Nanoscale Res. Lett.* **2014**, *9*, 625. [[CrossRef](#)] [[PubMed](#)]
67. Hsu, H.S.; Huang, J.C.A.; Huang, Y.H.; Liao, Y.F.; Lin, M.Z.; Lee, C.H.; Lee, J.F.; Chen, S.F.; Lai, L.Y.; Liu, C.P. Evidence of oxygen vacancy enhanced room-temperature ferromagnetism in Co-doped ZnO. *Appl. Phys. Lett.* **2006**, *88*, 242507. [[CrossRef](#)]
68. da Silva, R.T.; Mesquita, A.; de Zavallos, A.O.; Chiamonte, T.; Gratens, X.; Chitta, V.A.; Morbec, J.M.; Rahman, G.; García-Suárez, V.M.; Doriguetto, A.C.; et al. Multifunctional nanostructured Co-doped ZnO: Co spatial distribution and correlated magnetic properties. *Phys. Chem. Chem. Phys.* **2018**, *20*, 20257–20269. [[CrossRef](#)] [[PubMed](#)]
69. Shatnawi, M.; Alsmadi, A.M.; Bsoul, I.; Salameh, B.; Mathai, M.; Alnawashi, G.; Alzoubi, G.M.; Al-Dweri, F.; Bawa'aneh, M.S. Influence of Mn doping on the magnetic and optical properties of ZnO nanocrystalline particles. *Results Phys.* **2016**, *6*, 1064–1071. [[CrossRef](#)]

70. Mamani, N.C.; da Silva, R.T.; de Zevallos, A.O.; Cotta, A.A.C.; Macedo, W.A.D.; Li, M.S.; Bernardi, M.I.B.; Doriguetto, A.C.; de Carvalho, H.B. On the nature of the room temperature ferromagnetism in nanoparticulate co-doped ZnO thin films prepared by EB-PVD. *J. Alloys Compd.* **2017**, *695*, 2682–2688. [[CrossRef](#)]
71. Othman, A.A.; Osman, M.A.; Ibrahim, E.M.M.; Ali, M.A.; Abd-Elrahim, A.G. Mn-doped ZnO nanocrystals synthesized by sonochemical method: Structural, photoluminescence, and magnetic properties. *Mater. Sci. Eng. B* **2017**, *219*, 1–9. [[CrossRef](#)]
72. Martínez, B.; Sandiumenge, F.; Balcells, L.; Arbiol, J.; Sibieude, F.; Monty, C. Structure and magnetic properties of Co-doped ZnO nanoparticles. *Phys. Rev. B* **2005**, *72*, 165202. [[CrossRef](#)]
73. Wojnarowicz, J.; Kusnieruk, S.; Chudoba, T.; Gierlotka, S.; Lojkowski, W.; Knoff, W.; Lukaszewicz, M.I.; Witkowski, B.S.; Wolska, A.; Klepka, M.T.; et al. Paramagnetism of cobalt-doped ZnO nanoparticles obtained by microwave solvothermal synthesis. *Beilstein J. Nanotechnol.* **2015**, *6*, 1957–1969. [[CrossRef](#)] [[PubMed](#)]
74. Zhang, J.; Tse, K.; Wong, M.; Zhang, Y.; Zhu, J. A brief review of co-doping. *Front. Phys.* **2016**, *11*, 117405. [[CrossRef](#)]
75. Katayama-Yoshida, H.; Nishimatsu, T.; Yamamoto, T.; Orita, N. Codoping method for the fabrication of low-resistivity wide band-gap semiconductors in p-type GaN, p-type AlN and n-type diamond: Prediction versus experiment. *J. Phys. Condens. Matter* **2001**, *13*, 8901–8914. [[CrossRef](#)]
76. Eringen, A.C.; Maugin, G.A. *Electrodynamics of Continua I: Foundations and Solid Media*; Springer: New York, NY, USA, 1990; ISBN 978-1-4612-3226-1.
77. Jung, S.W.; An, S.J.; Yi, G.C.; Jung, C.U.; Lee, S.; Cho, S. Ferromagnetic properties of Zn_{1-x}Mn_xO epitaxial thin films. *Appl. Phys. Lett.* **2002**, *80*, 4561–4563. [[CrossRef](#)]
78. Jaćimović, J.; Micković, Z.; Gaál, R.; Smajda, R.; Vāju, C.; Sienkiewicz, A.; Forró, L.; Magrez, A. Synthesis, electrical resistivity, thermo-electric power and magnetization of cubic ZnMnO₃. *Solid State Commun.* **2011**, *151*, 487–490. [[CrossRef](#)]
79. Blasco, J.; García, J. Stable cubic spinels in the Zn–Mn–O system in air. *J. Solid State Chem.* **2006**, *179*, 2199–2205. [[CrossRef](#)]
80. Han, S.J.; Jang, T.H.; Kim, Y.B.; Park, B.G.; Park, J.H.; Jeong, Y.H. Magnetism in Mn-doped ZnO bulk samples prepared by solid state reaction. *Appl. Phys. Lett.* **2003**, *83*, 920–922. [[CrossRef](#)]
81. Christensen, A.N.; Ollivier, G. Hydrothermal preparation and low temperature magnetic properties of Mn(OH)₂. *Solid State Commun.* **1972**, *10*, 609–614. [[CrossRef](#)]
82. Norton, D.P.; Overberg, M.E.; Pearton, S.J.; Pruessner, K.; Budai, J.D.; Boatner, L.A.; Chisholm, M.F.; Lee, J.S.; Khim, Z.G.; Park, Y.D.; et al. Ferromagnetism in cobalt-implanted ZnO. *Appl. Phys. Lett.* **2003**, *83*, 5488–5490. [[CrossRef](#)]
83. Brumage, W.H.; Dorman, C.F.; Quade, C.R. Temperature-dependent paramagnetic susceptibilities of Cu²⁺ and Co²⁺ as dilute impurities in ZnO. *Phys. Rev. B Condens. Matter* **2001**, *63*, 104411. [[CrossRef](#)]
84. Cho, Y.M.; Choo, W.K.; Kim, H.; Kim, D.; Ihm, Y.E. Effects of rapid thermal annealing on the ferromagnetic properties of sputtered Zn_{1-x}(Co_{0.5}Fe_{0.5})_xO thin films. *Appl. Phys. Lett.* **2002**, *80*, 3358. [[CrossRef](#)]
85. Seidov, Z.; Açıkgöz, M.; Kazan, S.; Mikailzade, F. Magnetic properties of Co₃O₄ polycrystal powder. *Ceram. Int.* **2016**, *42*, 12928–12931. [[CrossRef](#)]
86. Singh, V.; Major, D.T. Electronic Structure and Bonding in Co-Based Single and Mixed Valence Oxides: A Quantum Chemical Perspective. *Inorg. Chem.* **2016**, *55*, 3307–3315. [[CrossRef](#)] [[PubMed](#)]
87. Mariappan, C.R.; Kumara, R.; Vijaya Prakash, G. Functional properties of ZnCo₂O₄ nano-particles obtained by thermal decomposition of a solution of binary metal nitrates. *RSC Adv.* **2015**, *5*, 26843–26849. [[CrossRef](#)]
88. Gupta, A.; Tiwari, S.D. Magnetic Properties of Undoped and Al doped Layered α-Co(OH)₂. *Phys. B Condens. Matter* **2017**, *525*, 21–25. [[CrossRef](#)]
89. Yan, L.; Ong, C.K.; Rao, X.S. Magnetic order in Co-doped and (Mn, Co) codoped ZnO thin films by pulsed laser deposition. *J. Appl. Phys.* **2004**, *96*, 508–511. [[CrossRef](#)]
90. Gu, Z.B.; Yuan, C.S.; Lu, M.H.; Wang, J.; Wu, D.; Zhang, S.T.; Zhu, S.N.; Zhu, Y.Y.; Chena, Y.F. Magnetic and transport properties of (Mn, Co)-codoped ZnO films prepared by radio-frequency magnetron cosputtering. *J. Appl. Phys.* **2005**, *98*, 053908. [[CrossRef](#)]
91. Gu, Z.-B.; Lu, M.-H.; Wang, J.; Du, C.-L.; Yuan, C.-S.; Wu, D.; Zhang, S.-T.; Zhu, Y.-Y.; Zhu, S.-N.; Chen, Y.-F. Optical properties of (Mn, Co) co-doped ZnO films prepared by dual-radio frequency magnetron sputtering. *Thin Solid Films* **2006**, *515*, 2361–2365. [[CrossRef](#)]

92. Du, C.L.; Gu, Z.B.; You, Y.M.; Kasim, J.; Yu, T.; Shen, Z.X.; Ni, Z.H.; Ma, Y.; Cheng, G.X.; Chen, Y.F. Resonant Raman spectroscopy of (Mn,Co)-codoped ZnO films. *J. Appl. Phys.* **2008**, *103*, 023521. [[CrossRef](#)]
93. Duan, L.B.; Rao, G.H.; Wang, Y.C.; Yu, J.; Wang, T. Magnetization and Raman scattering studies of (Co,Mn) codoped ZnO nanoparticles. *J. Appl. Phys.* **2008**, *104*, 013909. [[CrossRef](#)]
94. Nirmala, M.; Smitha, P.; Anukaliani, A. Optical and electrical properties of undoped and (Mn, Co) co-doped ZnO nanoparticles synthesized by DC thermal plasma method. *Superlattices Microstruct.* **2011**, *50*, 563–571. [[CrossRef](#)]
95. Nirmala, M.; Anukaliani, A. Synthesis and characterization of undoped and TM (Co, Mn) doped ZnO nanoparticles. *Mater. Lett.* **2011**, *65*, 2645–2648. [[CrossRef](#)]
96. Li, H.; Huang, Y.; Zhang, Q.; Qiao, Y.; Gu, Y.; Liu, J.; Zhang, Y. Facile synthesis of highly uniform Mn/Co-codoped ZnO nanowires: Optical, electrical, and magnetic properties. *Nanoscale* **2011**, *3*, 654–660. [[CrossRef](#)] [[PubMed](#)]
97. Inamdar, D.Y.; Lad, A.D.; Pathak, A.K.; Dubenko, I.; Ali, N.; Mahamuni, S. Ferromagnetism in ZnO Nanocrystals: Doping and Surface Chemistry. *J. Phys. Chem. C* **2010**, *114*, 1451–1459. [[CrossRef](#)]
98. Phan, L.; Vincent, R.; Cherns, D.; Dan, N.H.; Yu, S.C. Characterization of (Mn, Co)-Codoped ZnO Nanorods Prepared by Thermal Diffusion. *IEEE Trans. Magn.* **2009**, *45*, 2435–2438. [[CrossRef](#)]
99. Naeem, M.; Hasanain, S.K. Role of donor defects in stabilizing room temperature ferromagnetism in (Mn, Co) co-doped ZnO nanoparticles. *J. Phys. Condens. Matter* **2012**, *24*, 245305. [[CrossRef](#)] [[PubMed](#)]
100. Yin-Hua, Y.; Xi, C.Q. Infrared emissivities of Mn, Co co-doped ZnO powders. *Chin. Phys. B* **2012**, *21*, 124205. [[CrossRef](#)]
101. Sato, W.; Kano, Y.; Suzuki, T.; Nakagawa, M.; Kobayashi, Y. Local fields in Co and Mn Co-doped ZnO. *Hyperfine Interact.* **2016**, *237*, 28. [[CrossRef](#)]
102. Li, H.; Liu, H.; Zheng, Z.J. Magnetic behavior of Co–Mn co-doped ZnO nanoparticles. *Magn. Magn. Mater.* **2014**, *372*, 37–40. [[CrossRef](#)]
103. Neena, D.; Shah, A.H.; Deshmukh, K.; Ahmad, H.; Fu, D.J.; Kondamareddy, K.K.; Kumar, P.; Dwivedi, R.K.; Sing, V. Influence of (Co-Mn) co-doping on the microstructures, optical properties of sol-gel derived ZnO nanoparticles. *Eur. Phys. J. D* **2016**, *70*, 53. [[CrossRef](#)]
104. Sivaselvan, S.; Muthukumaran, S.; Ashokkumar, M. Influence of Co-doping on the structural, optical and morphological properties of Zn_{0.96}Mn_{0.04}O nanoparticles by sol-gel method. *Opt. Mater.* **2014**, *36*, 797–803. [[CrossRef](#)]
105. Abdullahi, S.S.; Köseog, Y.; Güner, S.; Kazan, S.; Kocaman, B.; Ndikilar, C.E. Synthesis and characterization of Mn and Co codoped ZnO nanoparticles. *Superlattices Microstruct.* **2015**, *83*, 342–352. [[CrossRef](#)]
106. Köseoğlu, Y. Fuel aided rapid synthesis and room temperature ferromagnetism of M_{0.1}Co_{0.1}Zn_{0.8}O (M = Mn, Ni, Fe and Cu) DMS nanoparticles. *Ceram. Int.* **2016**, *42*, 9190–9195. [[CrossRef](#)]
107. Pazhanivelu, V.; Blessington Selvadurai, A.P.; Zhao, Y.; Thiyagarajan, R.; Murugaraj, R. Room temperature ferromagnetism in Mn doped ZnO: Co nanoparticles by co-precipitation method. *Phys. B Condens. Matter* **2016**, *481*, 91–96. [[CrossRef](#)]
108. Pazhanivelu, V.; Blessington Selvadurai, A.P.; Murugaraj, R. Sintering Effect on Structural, Optical and Unusual Magnetic Behaviour in Zn_{0.95}Co_{0.05}O-Based DMS Materials. *J. Supercond. Nov. Magn.* **2015**, *28*, 2575–2581. [[CrossRef](#)]
109. Pazhanivelu, V.; Blessington Selvadurai, A.P.; Murugaraj, R. Room temperature magnetic behaviour of Mn codoping in ZnO: Co nanoparticles synthesized by co-precipitation method. *J. Mater. Sci. Mater. Electron.* **2018**, *29*, 3087–3094. [[CrossRef](#)]
110. Yakout, S.M.; El-Sayed, A.M. Synthesis, Structure, and Room Temperature Ferromagnetism of Mn and/or Co Doped ZnO Nanocrystalline. *J. Supercond. Nov. Magn.* **2016**, *29*, 1593–1599. [[CrossRef](#)]
111. Karthika, K.; Ravichandran, K. Enhancing the magnetic and antibacterial properties of ZnO nanopowders through Mn+Co doping. *Ceram. Int.* **2015**, *41*, 7944–7951. [[CrossRef](#)]
112. Sharma, D.; Jha, R. Transition metal (Co, Mn) co-doped ZnO nanoparticles: Effect on structural and optical properties. *J. Alloys Compd.* **2017**, *698*, 532–538. [[CrossRef](#)]
113. Khan, R.; de Araujo, C.I.L.; Khan, T.; Khan, A.; Ullah, B.; Fashu, S. Influence of oxygen vacancies on the structural, dielectric, and magnetic properties of (Mn, Co) co-doped ZnO nanostructures. *J. Mater. Sci. Mater. Electron.* **2018**, *29*, 9785–9795. [[CrossRef](#)]

114. Khan, R.; Fashu, Z.S.; Rehman, Y.U.; Khan, A.; Rahman, M.U. Structure and magnetic properties of (Co, Mn) co-doped ZnO diluted magnetic semiconductor nanoparticles. *J. Mater. Sci. Mater. Electron.* **2018**, *29*, 32–37. [[CrossRef](#)]
115. Li, G.R.; Qu, D.L.; Zhao, W.X.; Tong, Y.X. Electrochemical deposition of (Mn, Co)-codoped ZnO nanorod arrays without any template. *Electrochem. Commun.* **2007**, *9*, 1661–1666. [[CrossRef](#)]
116. Dai, J.; Meng, C.; Li, Q. First-principles study on the magnetism of Mn and Co codoped ZnO. *Phys. B Condens. Matter* **2013**, *409*, 5–9. [[CrossRef](#)]
117. Stashans, A.; Rivera, K. Electronic and Magnetic Properties of Co- and Mn-codoped ZnO by Density Functional Theory. *Chin. Phys. Lett.* **2016**, *33*, 097102. [[CrossRef](#)]
118. Liu, Z.; Yuan, X.; Yang, P. Investigation on electronic and magnetic properties of Co and Mn in ZnO with different doping types. *J. Magn. Magn. Mater.* **2018**, *461*, 1–5. [[CrossRef](#)]
119. Horikoshi, S.; Serpone, N. *Microwaves in Nanoparticle Synthesis: Fundamentals and Applications*; Wiley-VCH Verlag GmbH & Co. KGaA: Weinheim, Germany, 2013; ISBN 9783527331970.
120. Chikan, V.; McLaurin, E.J. Rapid Nanoparticle Synthesis by Magnetic and Microwave Heating. *Nanomaterials* **2016**, *6*, 85. [[CrossRef](#)] [[PubMed](#)]
121. Saleh, T.A.; Majeed, S.; Nayak, A.; Bhushan, B. Principles and Advantages of Microwave—Assisted Methods for the Synthesis of Nanomaterials for Water Purification. In *Advanced Nanomaterials for Water Engineering, Treatment, and Hydraulics*, 2nd ed.; Saleh, T.A., Ed.; IGI Global: Hershey, PA, USA, 2017; pp. 40–57; ISBN-10 1522521364.
122. Motshekga, S.C.; Pillai, S.K.; Ray, S.S.; Jalama, K.; Krause, R.W.M. Recent Trends in the Microwave-Assisted Synthesis of Metal Oxide Nanoparticles Supported on Carbon Nanotubes and Their Applications. *J. Nanomater.* **2012**, *2012*, 691503. [[CrossRef](#)]
123. Bilecka, I.; Niederberger, M. Microwave chemistry for inorganic nanomaterials synthesis. *Nanoscale* **2010**, *2*, 1358–1374. [[CrossRef](#)] [[PubMed](#)]
124. Gawande, M.B.; Shelke, S.N.; Zboril, R.; Varma, R.S. Microwave-Assisted Chemistry: Synthetic Applications for Rapid Assembly of Nanomaterials and Organics. *Acc. Chem. Res.* **2014**, *47*, 1338–1348. [[CrossRef](#)] [[PubMed](#)]
125. Koltsov, I.; Przeźniak-Welenc, M.; Wojnarowicz, J.; Rogowska, A.; Mizeracki, J.; Malysa, M.; Kimmel, G. Thermal and physical properties of ZrO₂-AlO(OH) nanopowders synthesised by microwave hydrothermal method. *J. Therm. Anal. Calorim.* **2017**, *13*, 2273–2284. [[CrossRef](#)]
126. Guenin, E. *Microwave Engineering of Nanomaterials: From Mesoscale to Nanoscale*, 1st ed.; Pan Stanford Publishing Pte. Ltd.: Boca Raton, FL, USA, 2016; ISBN 9789814669429.
127. Polshettiwar, V.; Nadagouda, M.N.; Varma, R.S. Microwaveassisted chemistry: A rapid and sustainable route to synthesis of organics and nanomaterials. *Aust. J. Chem.* **2009**, *62*, 16–26. [[CrossRef](#)]
128. Wojnarowicz, J.; Chudoba, T.; Majcher, A.; Łojkowski, W. Microwaves Applied to Hydrothermal Synthesis of Nanoparticles. In *Microwave Chemistry*, 1st ed.; Cravotto, G., Carnaroglio, D., Eds.; De Gruyter: Berlin, Germany; Boston, MA, USA, 2017; pp. 205–224; ISBN 9783110479935.
129. Łojkowski, W.; Leonelli, C.; Chudoba, T.; Wojnarowicz, J.; Majcher, A.; Mazurkiewicz, A. High-Energy-low-temperature technologies for the synthesis of nanoparticles: Microwaves and high pressure. *Inorganics* **2014**, *2*, 606–619. [[CrossRef](#)]
130. Kołodziejczak-Radzimska, A.; Jesionowski, T. Zinc Oxide-From Synthesis to Application: A Review. *Materials* **2014**, *7*, 2833–2881. [[CrossRef](#)] [[PubMed](#)]
131. Hasanpoor, M.; Aliofkhaeaei, M.; Delavari, H. Microwave-assisted Synthesis of Zinc Oxide Nanoparticles. *Proc. Mater. Sci.* **2015**, *11*, 320–325. [[CrossRef](#)]
132. Shao, D.; Wei, Q. Microwave-Assisted Rapid Preparation of Nano-ZnO/Ag Composite Functionalized Polyester Nonwoven Membrane for Improving Its UV Shielding and Antibacterial Properties. *Materials* **2018**, *11*, 1412. [[CrossRef](#)] [[PubMed](#)]
133. Rana, A.U.; Kang, M.; Kim, H.S. Microwave-assisted Facile and Ultrafast Growth of ZnO Nanostructures and Proposition of Alternative Microwave-assisted Methods to Address Growth Stoppage. *Sci. Rep.* **2016**, *6*, 24870. [[CrossRef](#)] [[PubMed](#)]
134. Rana, A.H.S.; Chang, S.B.; Kim, H.S. NH₄OH-Oriented and pH-Dependent Growth of ZnO Nanostructures via Microwave-Assisted Growth Method. *J. Nanosci. Nanotechnol.* **2018**, *18*, 2125–2127. [[CrossRef](#)] [[PubMed](#)]

135. Pimentel, A.; Ferreira, S.H.; Nunes, D.; Calmeiro, T.; Martins, R.; Fortunato, E. Microwave Synthesized ZnO Nanorod Arrays for UV Sensors: A Seed Layer Annealing Temperature Study. *Materials* **2016**, *9*, 299. [CrossRef] [PubMed]
136. Pimentel, A.; Nunes, D.; Duarte, P.; Rodrigues, J.; Costa, F.M.; Monteiro, T.; Martins, R.; Fortunato, E. Synthesis of Long ZnO Nanorods under Microwave Irradiation or Conventional Heating. *J. Phys. Chem. C* **2014**, *118*, 14629–14639. [CrossRef]
137. Barreto, G.P.; Morales, G.; Quintanilla Ma, L.L. Microwave Assisted Synthesis of ZnO Nanoparticles: Effect of Precursor Reagents, Temperature, Irradiation Time, and Additives on Nano-ZnO Morphology Development. *J. Mater.* **2013**, *2013*, 478681. [CrossRef]
138. Barreto, G.; Morales, G.; Cañizo, A.; Eyer, N. Microwave Assisted Synthesis of ZnO Tridimensional Nanostructures. *Proc. Mater. Sci.* **2015**, *8*, 535–540. [CrossRef]
139. Ghosh, S.; Chakraborty, J. Rapid synthesis of zinc oxide nanoforest: Use of microwave and forced seeding. *Mater. Res. Express* **2016**, *3*, 125004. [CrossRef]
140. Wojnarowicz, J.; Opalinska, A.; Chudoba, T.; Gierlotka, S.; Mukhovskiy, R.; Pietrzykowska, E.; Sobczak, K.; Lojkowski, W. Effect of water content in ethylene glycol solvent on the size of ZnO nanoparticles prepared using microwave solvothermal synthesis. *J. Nanomater.* **2016**, *2016*, 2789871. [CrossRef]
141. Wojnarowicz, J.; Chudoba, T.; Koltsov, I.; Gierlotka, S.; Dworakowska, S.; Lojkowski, W. Size control mechanism of ZnO nanoparticles obtained in microwave solvothermal synthesis. *Nanotechnology* **2018**, *29*, 065601. [CrossRef] [PubMed]
142. Mohammadi, E.; Aliofkhaezai, M.; Hasanpoor, M.; Chipara, M. Hierarchical and Complex ZnO Nanostructures by Microwave-Assisted Synthesis: Morphologies, Growth Mechanism and Classification. *Crit. Rev. Solid State Mater. Sci.* **2018**, *43*, 475–541. [CrossRef]
143. Majcher, A.; Wiejak, J.; Przybylski, J.; Chudoba, T.; Wojnarowicz, J. A novel reactor for microwave hydrothermal scale-up nanopowder synthesis. *Int. J. Chem. React. Eng.* **2013**, *11*, 361–368. [CrossRef]
144. Cravotto, G.; Carnaroglio, D. *Microwave Chemistry*, 1st ed.; De Gruyter: Berlin, Germany; Boston, MA, USA, 2017; ISBN 9783110479935.
145. Rinaldi, L.; Carnaroglio, D.; Rotolo, L.; Cravotto, G. A Microwave-Based Chemical Factory in the Lab: From Milligram to Multigram Preparations. *J. Chem.* **2015**, *2015*, 879531. [CrossRef]
146. Dąbrowska, S.; Chudoba, T.; Wojnarowicz, J.; Łojkowski, W. Current Trends in the Development of Microwave Reactors for the Synthesis of Nanomaterials in Laboratories and Industries: A Review. *Crystals* **2018**, *8*, 379. [CrossRef]
147. Dąbrowska, S.; Chudoba, T.; Wojnarowicz, J.; Łojkowski, W. Problems of exploitations of microwave reactors for nanoparticles synthesis. *J. Mach. Construct. Maint.* **2018**, *110*, 41–47.
148. Wojnarowicz, J.; Chudoba, T.; Gierlotka, S.; Lojkowski, W. Effect of Microwave Radiation Power on the Size of Aggregates of ZnO NPs Prepared Using Microwave Solvothermal Synthesis. *Nanomaterials* **2018**, *8*, 343. [CrossRef] [PubMed]
149. Wojnarowicz, J.; Mukhovskiy, R.; Pietrzykowska, E.; Kusnieruk, S.; Mizeracki, J.; Lojkowski, W. Microwave solvothermal synthesis and characterization of manganese-doped ZnO nanoparticles. *Beilstein J. Nanotechnol.* **2016**, *7*, 721–732. [CrossRef] [PubMed]
150. Wojnarowicz, J.; Kuśnieruk, S.; Chudoba, T.; Mizeracki, J.; Łojkowski, W. Microwave solvothermal synthesis of Co-doped ZnO nanoparticles. *Glass Ceram.* **2015**, *3*, 8–13.
151. Wojnarowicz, J.; Chudoba, T.; Gierlotka, S.; Sobczak, K.; Lojkowski, W. Size Control of Cobalt-Doped ZnO Nanoparticles Obtained in Microwave Solvothermal Synthesis. *Crystals* **2018**, *8*, 179. [CrossRef]
152. Lojkowski, W.; Gedanken, A.; Grzanka, E.; Opalinska, A.; Strachowski, T.; Pielaszek, R.; Tomaszewska-Grzeda, A.; Yatsunencko, S.; Godlewski, M.; Matysiak, H.; et al. Solvothermal synthesis of nanocrystalline zinc oxide doped with Mn²⁺, Ni²⁺, Co²⁺ and Cr³⁺ ions. *J. Nanopart. Res.* **2009**, *11*, 1991–2002. [CrossRef]
153. Pielaszek, R. FW15/45M method for determination of the grain size distribution from powder diffraction line profile. *J. Alloys Compd.* **2004**, *37*, 128–132. [CrossRef]
154. Nanopowder XRD Processor Demo, pre- α -ver.0.0.8, © Pielaszek Research. Available online: <http://science24.com/xrd/> (accessed on 10 January 2018).
155. FW1/5 4/5M Method of Evaluation of Grain Size Distribution by Powder Diffraction. Available online: <http://science24.com/fw145m/> (accessed on 10 January 2018).

156. Zhang, Q.; Park, K.; Cao, G. Synthesis of ZnO Aggregates and Their Application in Dye-sensitized Solar Cells. *Mater. Matters* **2014**, *5*, 32–39.
157. Poul, L.; Jouini, N.; Fiévet, F. Layered Hydroxide Metal Acetates (Metal = Zinc, Cobalt, and Nickel): Elaboration via Hydrolysis in Polyol Medium and Comparative Study. *Chem. Mater.* **2000**, *12*, 3123–3132. [[CrossRef](#)]
158. O’Keeffe, M.; Hyde, B.G. *Crystal Structures: I. Patterns and Symmetry*, 1st ed.; Mineralogical Society of America: Washington, DC, USA, 1996; ISBN 0939950405.
159. Rao, M.S.R.; Okada, T. *ZnO Nanocrystals and Allied Materials*; Springer: New Delhi, India, 2014; ISBN 978-81-322-1159-4.
160. Kück, S.; Werheit, H. *Non-Tetrahedrally Bonded Binary Compounds II*; Springer: Berlin/Heidelberg, Germany, 2000; ISBN 978-3-540-64966-3.
161. Sarbas, B.; Töpfer, W. *Mn Manganese*; Springer: Berlin/Heidelberg, Germany, 1993; ISBN 978-3-662-08907-1.
162. Saravanan, R. *Solid Oxide Fuel Cell (SOFC) Materials*; Materials Research Forum LLC: Millersville, PA, USA, 2018; ISBN 978-1-945291-50-0.
163. Olesik, J.W. Elemental analysis using ICP-OES and ICP/MS. *Anal. Chem.* **1991**, *63*, 12A–21A. [[CrossRef](#)]
164. Barsoum, M.W. *Fundamentals of Ceramics*, 1st ed.; Taylor & Francis Group: New York, NY, USA; Northampton, UK, 2002; ISBN 9780750309028.
165. Opalinska, A.; Malka, I.; Dzwolak, W.; Chudoba, T.; Presz, A.; Lojkowski, W. Size-dependent density of zirconia nanoparticles. *Beilstein J. Nanotechnol.* **2015**, *6*, 27–35. [[CrossRef](#)] [[PubMed](#)]
166. Kusnieruk, S.; Wojnarowicz, S.; Chodara, A.; Chudoba, T.; Gierlotka, S.; Lojkowski, W. Influence of hydrothermal synthesis parameters on the properties of hydroxyapatite nanoparticles. *Beilstein J. Nanotechnol.* **2016**, *7*, 1586–1601. [[CrossRef](#)] [[PubMed](#)]
167. Wejrzanowski, T.; Pielaszek, R.; Opalińska, A.; Matysiak, H.; Łojkowski, W.; Kurzydłowski, K.J. Quantitative methods for nanopowders characterization. *Appl. Surf. Sci.* **2006**, *253*, 204–208. [[CrossRef](#)]
168. Zając, M.; Gosk, J.; Grzanka, E.; Kamińska, M.; Twardowski, A.; Strojek, B.; Szyszko, T.; Podsiadło, S. Possible origin of ferromagnetism in (Ga,Mn)N. *J. Appl. Phys.* **2003**, *93*, 4715–4717. [[CrossRef](#)]
169. Zając, M.; Gosk, J.; Grzanka, E.; Stelmakh, S.; Palczewska, M.; Wyszmołek, A.; Korona, K.; Kamińska, M.; Twardowski, A. Ammonothermal synthesis of GaN doped with transition metal ions (Mn, Fe, Cr). *J. Alloys Compd.* **2008**, *456*, 324–338. [[CrossRef](#)]
170. Lawniczak-Jablonska, K.; Wolska, A.; Klepka, M.T.; Kret, S.; Gosk, J.; Twardowski, A.; Wasik, D.; Kwiatkowski, A.; Kurowska, B.; Kowalski, B.J.; et al. Magnetic properties of MnSb inclusions formed in GaSb matrix directly during molecular beam epitaxial growth. *J. Appl. Phys.* **2011**, *109*, 074308. [[CrossRef](#)]
171. Gaj, J.A.; Planel, R.; Fishman, G. Relation of magneto-optical properties of free excitons to spin alignment of Mn²⁺ ions in Cd_{1-x}Mn_xTe. *Solid State Commun.* **1979**, *29*, 435–438. [[CrossRef](#)]
172. Gaj, J.A. On the physical meaning of the modified Brillouin function. *Acta Phys. Pol.* **1988**, *73*, 463–466.

